POLITECNICO DI MILANO

Dottorato in Ingegneria Aerospaziale

Cycle XXIV

INDEPENDENT FIELDS FULL POTENTIAL FORMULATION FOR AEROELASTIC ANALYSES

Supervisor:
Prof. Paolo MANTEGAZZA
Director of Ph.D. School:
Prof. Sergio RICCI

Ph.D. Thesis of:
Andrea PARRINELLO
Matr. 738534

March 2012

Abstract

The thesis presents a full potential model for non isentropic unsteady transonic flows based on an independent approximation of the density and velocity potential fields. The formulation retains the advantage of the existence of a velocity potential while granting a unique solution by combining a correction of the stagnation pressure behind a shock with a new form of Kutta condition. An alternative ALE formulation ensures that mass conservation and Bernoulli equation are satisfied in a domain moving with a generic velocity field avoiding the need of enforcing any geometric conservation law. The solution procedure relies on an unstructured, node based, finite volume approximation, with linear|quadratic shape functions and non reflecting far field boundary conditions. An improved upwind density biasing stabilizes the solution in supersonic regions. A special tool to generate the wake discretization within generic unstructured meshes leads to an easy adoption of potential flows for complex configurations. Time marching solutions are dealt using first|second order implicit schemes, whose unconditional linearized stability properties are demonstrated for sub-supersonic asymptotic conditions. Numerical results validate the method and show that it can model Euler solutions more accurately than an isentropic full potential formulation, for both steady and unsteady conditions. Applications to asymptotically supersonic flows, flutter analyses and static trim evaluations complete the numerical validation.

Sommario

Il presente lavoro descrive un modello a potenziale completo instazionario non isentropico basato su una approssimazione indipendente dei campi di densità e potenziale velocità. La formulazione conserva il vantaggio dell'esistenza di un potenziale velocità e garantisce l'unicità della soluzione combinando una correzione della pressione di ristagno a valle di un urto con una nuova forma della condizione di Kutta. Una formulazione ALE alternativa assicura che il bilancio di massa e il teorema di Bernoulli siano soddisfatti in un dominio dotato di un campo di moto generico rimuovendo la necessità di imporre una legge geometrica di conservazione. La procedura risolutiva si realizza per mezzo di un'approssimazione a volumi finiti non strutturati centrati ai nodi con funzioni di forma lineari|quadratiche e condizioni di non riflessione al contorno esterno. Un'efficace tecnica di dissimmetrizzazione della funzione densità stabilizza la soluzioni nelle regioni supersoniche. Un apposito strumento di generazione di scie su griglie non strutturate permette di trattare geometrie complesse e di impiegare griglie preesistenti. Soluzioni a tempo discreto sono trattate con schemi impliciti del primo|secondo ordine le cui caratteristiche di incondizionata stabilità sono dimostrate per condizioni asintotiche sub-supersoniche. I risultati numerici dimostrano l'efficacia del metodo e mostrano come questo riesca a modellare soluzioni Euleriane più accuratamente rispetto a un modello a potenziale isentropico sia per condizioni stazionarie che instazionarie. Applicazioni a flussi asintotici supersonici, analisi di stabilità aeroelastica e analisi di equilibrio statico completano la validazione numerica.

I particularly wish to thank Professor Mantegazza. His support, encouragement and ideas were valued.

Special thanks are also due to Giulio Romanelli for his patience and for supplying alternative numerical solutions.

Contents

List of Figures

List of Tables

Nomenclature

$*_\infty$	Asymptotic value of $*$
$*_t$	Time derivative of $*$
α	Angle of attack (deg)
Δ	Increment operator
γ	Heat capacity ratio
$\nabla\cdot$	Divergence operator
∇	Gradient operator
ϕ	Velocity potential (m^2/s)
ρ	Density (kg/m^3) and dimensionless density
CFL	Courant, Friedrichs and Lewy number
φ	Reduced velocity potential: ϕ/V_∞ (m)
c	Speed of sound (m/s)
C_L	Lift coefficient
C_p	Pressure coefficient
c_v	Specific heat at constant volume $(J/kg/K)$
H	Total enthalpy (m^2/s^2)
h	Spatial discretization (m)
K	Entropy index: p/ρ^γ
k	Reduced entropy index: K/K_∞

M	Mach number
M^*	Critical Mach number
p	Pressure (N/m^2)
p_0	Stagnation pressure (N/m^2)
s	Entropy ($J/kg/K$)
V	Velocity vector (m/s)

Chapter 1

Introduction

Modern aircrafts operate at speeds where aeroelastic instabilities are more likely to occur. To successfully analyze such aeroelastic phenomena motion dependent aerodynamic loads must be accurately predicted. Since many critical aeroelastic phenomena occur at transonic speeds, an aerodynamic method that can properly model shock waves and their unsteady motions must be used.

The potential flow approximation has been the dominating model for transonic aerodynamics for many years. It can be effectively used in aerodynamic design and analysis. Because of its comparatively small computational cost it remains of interest in multidisciplinary methodologies, for conceptual and preliminary design phases especially. Through the 1990s and 2000s, research and development on potential flow lost appeal in favor of Euler and Navier-Stokes solvers, the speed and memory capability of new computers making their use affordable more and more. Nonetheless, significant interest in FP solvers still persists. The shorter computational time required by FP solutions makes them appealing for aircraft conceptual and preliminary design phases and for linearized aeroelastic analyses. So, even though FP solutions cannot be as accurate as Euler ones, the quintessence of the physics of an inviscid flow can be captured anyway. Furthermore, FP solutions can be used as starters of Euler|Navier-Stokes flow solvers, significantly reducing the iterations required for convergence.

Interest in nonlinear potential flow analyses for the investigation of realistic transonic problems surged in the early 1970s. Initially, the solution of the Transonic Small Disturbance (TSD) equation was addressed. Along that line, one of the first viable solution schemes was developed by Murman and Cole [1] in 1971. They made an important observation concerning sub|supersonic domains by acknowledging the need of using centered differences within subsonic regions and backward differences within supersonic regions.

After Murman and Cole original paper, other researchers presented numerical methods for the solution of transonic flows. Steger and Lomax [2] introduced a solution based on relaxation with successive over relaxations (SOR). Garabedian and Korn [3] developed a second order accurate version of Murman and Cole scheme based on the Full Potential (FP) equation in non-conservative form. Ballhaus and Bailey [4] and Bailey and Steger [5] solved transonic flows of real wings using the TSD equation.

In 1974, Jameson [6] devised a more flexible approach better caring of the local flow direction, the so called Jameson's rotated difference scheme.

Then Murman [7] showed that the potential equation had to be solved in conservation form to correctly satisfy jump conditions. In fact Murman solved the TSD equation using a non-conservative form but introduced a shock-point differencing operator. A year later Jameson [8] solved the FP equation in full conservation form, applying an artificial viscosity to the difference scheme used for supersonic regions.

Work using the finite element method took place during the 1970s too, albeit at a slightly slower pace. Few of the first transonic flow computations based on finite elements appeared in 1976 by Glowinsky et al. [9] and Ecer and Akay [10]. The first structured finite volume calculations followed by Jameson and Caughey [11] in 1977.

A different solution technique for the FP equation was presented in 1978 by Hafez et al. [12]. The conservative form of the FP equation was solved using artificial compressibility, whereas density was modified in regions of supersonic flow to provide an appropriate upwinding. This scheme was called density biasing.

In 1979 Jameson [13] gained further efficiency by applying a multigrid technique to the conservative FP equation. The increase in efficiency was confirmed by Boerstoel [14], who remarked that the shock position was not efficiently updated by the multigrid method. Different multigrid strategies and smoothing operators were extensively discussed by Van der Wees et al. [15].

The artificial compressibility technique was widely used by the early 1980s, when a new upwinding concept was introduced, called flux biasing or flux upwinding. Flux biasing helped capturing shock locations more accurately and eliminated most of the oscillations occurring around the related discontinuities. The idea was initially developed in 1980 by Engquist and Osher [16]. Early applications to the FP equation were presented by Boerstoel [14] (1982) and Osher [17] (1982). Flux biasing and density biasing schemes were compared by Volpe and Jameson [18].

In 1995 Holst [19] developed an FP flow solver using the Chimera approach. The algorithm can be applied to the three dimensional flow over wings or wing/body geometries. An inner grid is used to describe the wing/body surface, while an outer grid describes the far field region. The grids can overlap, taking advantage of the flexibility of Chimera grids.

In 1997 R. E. Neel [20] claimed the first unstructured finite volume FP solver for cell-centered meshes.

As fast and reliable Euler solutions became routinely available for transonic flow calculations, it was found that Full Potential (FP) solutions were seriously in error when shocks became even moderately strong. Both shock strength and position were wrong and the magnitude of the related errors could have been significant. The inaccuracies of an FP model in predicting transonic aerodynamic loads is primarily a consequence of neglecting the jump in entropy that a fluid particle experiences as it crosses a shock. FP formulations allow a shock discontinuity to appropriately occur for mass and energy, but the shock remains isentropic and the momentum balance is not satisfied across it. Therefore, the calculated shock waves can have a wrong strength and location. One of the first analyses of the differences between Rankine-Hugoniot (R-H) and isentropic jump characteristics was presented by Steger and Baldwin [21, 22]. Further analyses of the isentropic jump relations were carried out by Van der Vooren and Slooff [23] and Murman and Cole [24]. Those studies were primarily concerned with drag prediction under isentropic assumptions.

When shocks appear in transonic flow fields, the aerodynamic loads predicted using an FP can even be multivalued. Multiple solutions of the potential equation were first observed in two dimensions by Steinhoff and Jameson [25]. Salas and Gumbert [26] showed that the phenomenon is not confined to a particular airfoil or flow condition. Boundary layer corrections can also stabilize potential calculations.

Through the 80s, as Euler solutions began showing the FP inaccuracies in predicting transonic aerodynamic loads, many researchers devoted much energy to the formulation of numerical schemes aimed at correcting the related transonic results, mainly for steady flows though. Klopfer and Nixon [27] examined possible jump formulations and showed that a potential jump which conserves momentum instead of energy is much closer to the actual R-H jump condition. Lucchi [28] changed the steady Kutta condition in an iteration way with Neumann-type boundary conditions at a flow slit at the body trailing edge. Hafez and Lovell [29] presented a method for modeling entropy jumps across shocks in steady potential flows. Whitlow, Hafez and Osher [30] extended their method to unsteady flows but, because of the use of the usual Kutta condition, their correction technique showed ineffective. Voss and Wegner [31] well understood the role of the entropy for the flow angle at the trailing edge.

An FP formulation prevents the proper entropy and vorticity production at the shock surface but these phenomena can be neglected for a moderate upstream Mach range. The entropy jump through a shock can be shown to be proportional to the third power of its intensity [32], $I = p_2/p_1 - 1$

$$\Delta s = \frac{c_p}{12\gamma^3} (\gamma + 1) (\gamma - 1) I^3 + O\left(I^4\right) . \tag{1.1}$$

Thus the entropy production is relatively negligible for weak shocks, so a potential model represents an acceptable and effective approximation. Indeed, despite the intrinsic differences between an isentropic and a R-H shock, FP formulations lead to non-lifting transonic results which are very close to Euler calculations. This proves that an isentropic shock can be a good approximation of the real shock. The situation is much different for lifting cases. The inaccuracy of the FP model in predicting transonic aerodynamic loads may become considerable. The wake treatment is the keystone for possible improvements. It ensures an appropriate pressure balance at the trailing edge and determines the amount of vorticity that leaves the body. Usually the wake surface is a discontinuity for the potential function and the Kutta condition imposes the continuity of both the pressure and, because of the isentropic assumption, the density across it. However, in its usual form, the wake condition cannot take into account the variation of stagnation pressure due to a shock on the body, thus leading to an incorrect pressure balance at the trailing edge with a consequently wrong shock position. The present work introduces a non-isentropic Bernoulli equation leading to a non-isentropic wake equation.

An important consideration when simulating fluid flow problems by any numerical method is the choice of an appropriate kinematical description of the flow field. The algorithms of continuum mechanics make use of three distinct types of description of motion: the Lagrangian description, the Eulerian description and the Arbitrary Lagrangian Eulerian (ALE) description.

Lagrangian algorithms, in which each individual node of the computational mesh follows the associated material particle during motion, are mainly used in structural mechanics. Classical applications of the Lagrangian description in large deformation problems are the simulation of vehicle crash tests and the modeling of metal forming operations. Numerical solutions are often characterized by large displacements and deformations and history-dependent constitutive relations are employed to describe elasto-plastic and visco-plastic material behavior. The Lagrangian description allows easy tracking of free surfaces and interfaces between different materials. Its weakness is its inability to follow large distortions of the computational domain without recourse to frequent remeshing operations.

Eulerian algorithms are widely used in fluid mechanics. Here, the computational mesh is fixed and the fluid moves with respect to the grid. The Eulerian formulation facilitates the treatment of large distortions in the fluid motion. Its handicap is the difficulty to follow free surfaces and interfaces between different materials or different media (e.g., fluid-solid interfaces).

ALE algorithms are particularly useful in flow problems involving large distortions in the presence of mobile and deforming boundaries. Typical examples are problems describing the interaction between a fluid and a flexible structure. The key idea in the ALE formulation is the introduction of a computational mesh which can move with a velocity independent of the velocity of the material particles. With this additional freedom with respect to the Eulerian and Lagrangian descriptions, the ALE method succeeds to a certain extend in minimizing the problems encountered in the classical kinematical descriptions, while combining at best their respective advantages. The ALE formulation seems the best choice for typical aeronautics applications where the vehicle deformation must be taken in to account for a proper evaluation of the fluid-solid interaction.

The present work introduces an alternative ALE formulation which ensures the proper mass conservation in a domain moving with a generic velocity field avoiding the need of monitoring the divergence of the motion.

When the unsteady solutions of interest are mainly aimed at linearized transonic flutter calculations the ALE formulation can be taken to the limit of an unmoving mesh, so producing a transpiration formulation at the body boundary allowing to deal with the related analyses using fixed meshes.

The presented formulation is based on an independent approximations of the density and potential fields that satisfy mass conservation and Bernoulli equation. Such a formulation was first sketched in [33] and rediscovered in [34] and [35]. The nonlinear ordinary differential equations in time resulting from a first|second order node centered unstructured finite volume space discretization are solved through an implicit time integration. The use of non-reflecting far field boundary conditions allows a relatively limited calculation domain. An improved upwind technique is used to better establish the right sub-supersonic dependence and allows to treat both subsonic and supersonic asymptotic conditions. The resulting linearized implicit scheme is proven to be unconditionally stable for sub-supersonic asymptotic solutions with embedded shocks.

The following sections detail the proposed approach and its implementation. Finally, numerical results demonstrate how the solutions thus obtained tend to better match those of an Euler formulation and show the effectiveness of the method in aeroelasticity.

Chapter 2

Model

2.1 Non Isentropic ALE Potential Flow Model

The present work is aimed to modelling attached flows past aerodynamic bodies at high Reynolds numbers. These circumstances ensure thin boundary layers and narrow vortical regions. The absolute motion field of such a flow can be suitably defined by a discontinuous velocity potential ϕ,

$$\vec{V} = \nabla\phi, \tag{2.1}$$

where the vorticity bounded to lines|surfaces is related to the jump of ϕ across them. This is the so-called quasi-potential flow [36]. Assuming the viscous stress and the heat sources to be negligible, the governing equations of the flow are [32]:

- the continuity equation,

$$\frac{\partial\rho}{\partial t} + \nabla\cdot(\rho\nabla\phi) = 0, \tag{2.2}$$

- Bernoulli theorem,

$$\frac{\partial\phi}{\partial t} + H - H_\infty = 0. \tag{2.3}$$

Both the potential function ϕ and the density function ρ can be defined on a reference domain R_G moving according to an absolute velocity field $\vec{V}_G$ on a spatial domain R_g.

Let us define the integral form of the continuity equation, *i.e.* eq. 2.2, in the fixed spatial domain R_g:

$$\int_v \frac{\partial \rho}{\partial t} dv + \int_v \nabla \cdot \left(\rho \vec{V}\right) dv = 0. \tag{2.4}$$

Defining the total time derivative with respect to R_G as:

$$\frac{d*}{dt} = \frac{\partial *}{\partial t} + \nabla * \cdot \vec{V}_G, \tag{2.5}$$

and applying the divergence theorem the continuity equation, eq. 2.4, becomes:

$$\int_v \left(\frac{d\rho}{dt} - \nabla \rho \cdot \vec{V}_G\right) dv + \int_\gamma \rho \vec{V} \cdot \vec{n} d\gamma = 0, \tag{2.6}$$

which represents the here proposed ALE formulation. Recalling that [32]

$$\frac{d(dv)}{dt} = \nabla \cdot \vec{V}_G dv, \tag{2.7}$$

where $\vec{V}_G$ is the transport velocity of the elementary volume being followed, the time derivative of the generic mass element becomes:

$$\frac{d}{dt}(\rho dv) = \frac{d\rho}{dt} dv + \rho \nabla \cdot \vec{V}_G dv. \tag{2.8}$$

Using it in combination with equation 2.6 we obtain:

$$\begin{aligned} \int_v \frac{d}{dt}(\rho dv) - \int_v \rho \nabla \cdot \vec{V}_G dv - \int_v \nabla \rho \cdot \vec{V}_G dv + \int_\gamma \rho \vec{V} \cdot \vec{n} d\gamma &= \\ \frac{d}{dt} \int_v \rho dv - \int_v \nabla \cdot \left(\rho \vec{V}_G\right) dv + \int_\gamma \rho \vec{V} \cdot \vec{n} d\gamma &= 0 \end{aligned} \tag{2.9}$$

So, the usual ALE formulation is obtained,

$$\frac{d}{dt} \int_v \rho dv + \int_\gamma \rho \left(\vec{V} - \vec{V}_G\right) \cdot \vec{n} d\gamma = 0. \tag{2.10}$$

The proposed ALE formulation, which leads to eq. 2.6, is independent from the time derivative of the control volume. The time derivative appears outside the integral operator in the usual ALE formulation, eq. 2.10, while remains inside in eq. 2.6.

The Bernoulli theorem, eq. 2.3, in the spatial domain R_g with the fluid at rest is:

$$\frac{\partial\phi}{\partial t}+\frac{1}{2}\left|\nabla\phi\right|^2+\frac{c_\infty^2}{\gamma-1}\left(\left(\frac{\rho}{\rho_\infty}\right)^{\gamma-1}-1\right)=0. \tag{2.11}$$

Applying the total time derivative, eq. 2.5, to the potential function the ALE form,

$$\frac{d\phi}{dt}-\nabla\phi\cdot\vec{V}_G+\frac{1}{2}\left|\nabla\phi\right|^2+\frac{c_\infty^2}{\gamma-1}\left(\left(\frac{\rho}{\rho_\infty}\right)^{\gamma-1}-1\right)=0. \tag{2.12}$$

The related integral form,

$$\int_v\left(\frac{d\phi}{dt}-\nabla\phi\cdot\vec{V}_G+H-H_\infty\right)dv=0, \tag{2.13}$$

is obtained, in which the convected reference frame is treated as for eq. 2.6. Using the time derivative of the elementary mass, eq. 2.8, the alternative integral ALE form can be obtained,

$$\frac{d}{dt}\int_v\phi dv+\int_v\left(H-H_\infty\right)dv-\int_v\nabla\cdot\left(\phi\vec{V}_G\right)dv, \tag{2.14}$$

which is akin to eq. 2.10, even if it is not a balance equation. ALE forms of the Bernoulli theorem can be applied to a motion field characterized by an asymptotic velocity $\vec{V}_\infty$ by expressing the potential function as:

$$\phi=\varphi+\vec{V}_\infty\cdot\vec{X} \tag{2.15}$$

and modifying the asymptotic total enthalpy H_∞. So, the time derivative of the potential becomes:

$$\frac{d\phi}{dt}=\frac{d\varphi}{dt}+\vec{V}_\infty\cdot\vec{V}_G. \tag{2.16}$$

The proposed ALE formulation will be preferred because it provides the same scheme for accounting of a moving grid R_G and because frees from any limitation from the mesh motion to grant Geometric Conservation Law (GCL) [37]. So, in order to avoid any numerical complication related to the domain movement, the proposed ALE formulation, in the form of eq. 2.6 and eq. 2.13, will be implemented.

Starting from the ALE forms of the continuity equation, eq. 2.6, and Bernoulli theorem, eq. 2.13, an entropy correction model is now proposed. The potential formulation does not admit non-homentropic conditions. First, according to Crocco's theorem, an entropy gradient implies vorticity in the motion field and so prevents the existence of a velocity potential. Moreover, terms related to the entropy gradient and to the vorticity, which appear in the momentum equation, are not state functions and so they cannot be easily integrated through a generic path to obtain a scalar equation, *i.e.* a "special" Bernoulli theorem. To tackle such a problem the motion field can be divided in two regions (fig. 2.1): a layer covering the body-wake surface, in which the flow can be non-homentropic, and a potential region which embeds the layer.

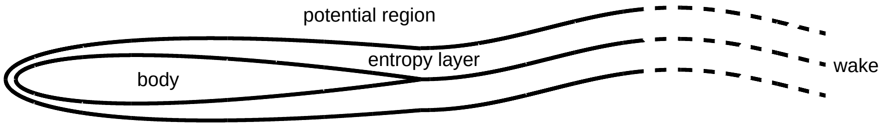

Figure 2.1: Domain decomposition

According the above remarks, the Bernoulli theorem, eq. 2.3, is strictly applicable only in the potential region. However, for relatively thin entropy layers, the velocity potential can be used for the whole domain and the entropy gradient that appears in the momentum equation can be neglected. These assumptions lead to a non isentropic approximation of the Bernoulli theorem,

$$\frac{d\phi}{dt} - \nabla\phi \cdot \vec{V}_G + \frac{1}{2}\left|\nabla\phi\right|^2 + \frac{c_\infty^2}{\gamma - 1}\left(\frac{K}{K_\infty}\left(\frac{\rho}{\rho_\infty}\right)^{\gamma-1} - 1\right) = 0, \tag{2.17}$$

where

$$K = \frac{p}{\rho^\gamma} = e^{s/c_v} = p_0^{1-\gamma}. \tag{2.18}$$

Then, the related ALE entropy transport equation is:

$$\frac{dK}{dt} - \nabla K \cdot \vec{V}_G + \nabla K \cdot \nabla\phi = 0, \tag{2.19}$$

which must also be applied within the entropy layer. Eq. 2.19 allows to convect the entropy produced by attached upstream shocks, so that the wake becomes a discontinuity for the entropy function. In order to freely satisfy the mass conservation across the wake, the pressure continuity between the lower (l) and upper (u) side of this line|surface must be imposed,

$$\Delta\left(K\rho^\gamma\right) = 0, \tag{2.20}$$

where the jump operator across the wake, $\Delta * = *_u - *_l$, appears. So the wake becomes a discontinuity for the density also. Writing the above Bernoulli theorem, eq. 2.17, across the wake the desired non isentropic ALE wake equation is obtained:

$$\frac{d\Delta\phi}{dt} - \nabla(\Delta\phi)\cdot\vec{V}_G + \frac{1}{2}\Delta\left|\nabla\phi\right|^2 + \frac{c_\infty^2}{(\gamma-1)\,K_\infty\rho_\infty^{\gamma-1}}\Delta\left(K\rho^{\gamma-1}\right) = 0. \quad (2.21)$$

Eqs. 2.2, 2.17, 2.19, 2.20 and 2.21 do not imply dissipative phenomena, so, when a shock occurs, an entropy jump related to the shock strength must be introduced in the entropy layer using the Rankine-Hugoniot (R-H) relation [32],

$$k_{\text{shock}} = \frac{K_2}{K_1} = \left(\frac{p_{02}}{p_{01}}\right)^{1-\gamma} = \frac{p_2}{\rho_2^\gamma}\frac{\rho_1^\gamma}{p_1} = \frac{2\gamma M_1^2 - (\gamma-1)}{\gamma+1}\left(\frac{2+(\gamma-1)\,M_1^2}{(\gamma+1)\,M_1^2}\right)^\gamma, \quad (2.22)$$

where 1 and 2 denote an upstream and downstream shock position respectively. To properly model the entropy jump at a moving shock the R-H relation, eq. 2.22, must be applied using an appropriate upstream Mach definition,

$$M_1 = \frac{V_1 - V_s}{c_1}, \quad (2.23)$$

which requires a jump model allowing to estimate the shock velocity V_s. The Prandtl relation [32],

$$M_1^* M_2^* = 1, \quad (2.24)$$

leads to a closed-form solution for the R-H shock velocity,

$$V_s = V_1 - \frac{\gamma+1}{4}(V_1 - V_2) - \sqrt{c_1^2 + \left(\frac{\gamma+1}{4}(V_1 - V_2)\right)^2}. \quad (2.25)$$

While the isentropic jump condition [21, 22],

$$\left(1 - \frac{\gamma-1}{\gamma+1}M_1^{*2}\right)^{\frac{1}{\gamma-1}} M_1^* = \left(1 - \frac{\gamma-1}{\gamma+1}M_2^{*2}\right)^{\frac{1}{\gamma-1}} M_2^*, \quad (2.26)$$

requires a numerical technique for the estimation of the shock velocity. In order to avoid such a trouble an acceptable good compromise is provided by Guderley [38] closed-form shock relation for small perturbations,

$$M_1^* + M_2^* = 2, \quad (2.27)$$

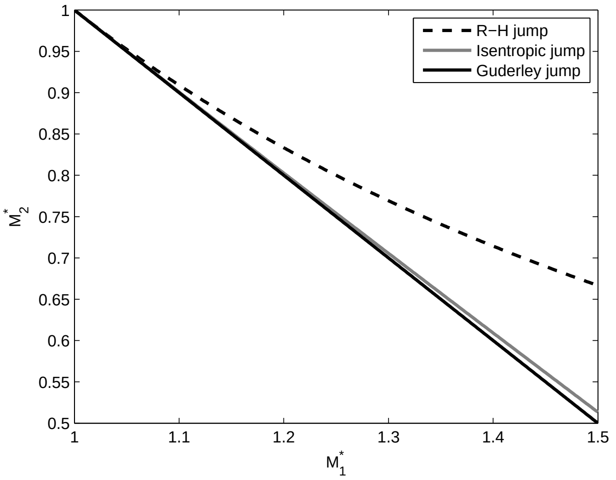

Figure 2.2: Shock relations

which, as shown in Figure 2.2, closely approximates the isentropic relation. From Guderley relation, eq. 2.27, the following shock velocity estimation is obtained,

$$V_s = \frac{V_1 + V_2}{2} - \sqrt{\frac{2}{\gamma+1}c_\infty^2 + \frac{\gamma-1}{\gamma+1}V_\infty^2}. \tag{2.28}$$

The velocity estimation, eq. 2.28, can be used in the R-H relation, eq. 2.22, through the upstream Mach definition, eq. 2.23. The entropy transport equation, eq. 2.31, and the shock velocity estimation, eq. 2.28, allow to apply an unsteady correction to the FP model.

All of the above equations are then adimensionalized with respect to the asymptotic values: ρ_∞, V_∞ and K_∞, while keeping lengths as dimensional quantities. So, denoting dimensional quantities with the suffix d, we define the following adimensionalized terms: $\rho = \rho_d/\rho_\infty$, $\varphi = \phi_d/V_\infty$, $k = K_d/K_\infty$, $t = V_\infty t_d$, $\vec{V}_G = \vec{V}_G/V_\infty$. Then equations 2.6, 2.17, 2.19, 2.20 and 2.21 become:

$$\rho_t - \nabla\rho\cdot\vec{V}_G + \nabla\cdot(\rho\nabla\varphi) = 0, \tag{2.29}$$

$$\varphi_t - \nabla\varphi\cdot\vec{V}_G + \frac{1}{2}|\nabla\varphi|^2 + \frac{M_\infty^{-2}}{\gamma-1}\left(k\rho^{\gamma-1} - 1\right) = 0, \tag{2.30}$$

$$k_t - \nabla k\cdot\vec{V}_G + \nabla k\cdot\nabla\varphi = 0, \tag{2.31}$$

$$\Delta\left(k\rho^\gamma\right) = 0, \tag{2.32}$$

$$\Delta\varphi_t - \Delta(\nabla\varphi)\cdot\vec{V}_G + \frac{1}{2}\Delta|\nabla\varphi|^2 + \frac{M_\infty^{-2}}{\gamma-1}\Delta\left(k\rho^{\gamma-1}\right) = 0 \tag{2.33}$$

with $M = M_\infty \left|\nabla\varphi\right| / \sqrt{k\rho^{\gamma-1}}$ and $C_p = 2\left(k\rho^\gamma - 1\right) / \left(\gamma M_\infty^2\right)$.

The scalar equations 2.29, 2.30 and 2.31, the wake conditions, eqs. 2.32 and 2.33, and the shock condition, eq. 2.22, combined with the shock velocity estimation, eq. 2.28, in the independent unknowns ρ, φ and k, constitute our FP model.

The most common strategy adopted so far to solve potential flows is to evaluate the density using Bernoulli equation, eq. 2.3,

$$\rho = \left[1 - \frac{\gamma-1}{2} M_\infty^2 \left(2\varphi_t + \left|\nabla\varphi\right|^2 - 1\right)\right]^{\frac{1}{\gamma-1}}, \tag{2.34}$$

substituting it in the mass conservation, eq. 2.2. This results in a conservative second-order differential equation in the unknown φ only. With a mechanical analogy φ can be identified as a degree of freedom function while the pair ρ-φ can be interpreted as state functions. So the two-field approach corresponds to formulating the problem in state space form directly. As hinted at already, the use of two independent approximations for ρ and φ to solve eqs. 2.2 and 2.3 was likely first proposed by Chipman [33] for unsteady, non lifting, structured 2D profiles. Nonetheless, such a formulation seems to have been little used, till the recent appearance of the unsteady, unstructured finite volume implementations of [34, 39, 40]. The two-field approach considerably simplifies the development of a numerical approximation, leading to a robust resolution scheme. It is also fundamental for an easy application of the modified FP model just presented, making it closer to the physics of the problem, for both steady and unsteady flows. The entropy production alters the momentum equation, leading to a non isentropic Bernoulli equation, eq. 2.30, and consequently to a non isentropic wake condition, eq. 2.33, while preserving mass conservation, eq. 2.29. Moreover, the two-field approach simplifies the development of a numerical *upwind*, needed to stabilize solution with shocks.

A robust unsteady FP solver should ensure unique and physically sound solutions. The satisfaction of such a desirable property has been verified though a large set of numerical verifications and afterward justified as hereafter said. Laitone [41, 42] derived a condition for the limiting velocity expected to occur over an airfoil at transonic speeds. For that he used a parameter defined by the ratio of the static pressure behind the shock, p_2, to the stagnation pressure ahead of the shock, p_{01}. For R-H shocks one obtains [32]:

$$\left(\frac{p_2}{p_{01}}\right)_{\text{R-H}} = \frac{p_2}{p_{02}}\frac{p_{02}}{p_{01}} = \left(1 + \frac{\gamma-1}{2} M_2^2\right)^{\frac{\gamma}{1-\gamma}} k_{\text{shock}}^{\frac{1}{1-\gamma}}. \tag{2.35}$$

For isentropic shocks, instead, the constant stagnation pressure leads to:

$$\left(\frac{p_2}{p_{01}}\right)_i = \left(\frac{p_2}{p_{02}}\right)_i = \left(1 + \frac{\gamma - 1}{2}\left(M_2\right)_i^2\right)^{\frac{\gamma}{1-\gamma}}. \tag{2.36}$$

The proposed model is equivalent to keeping the shock isentropic while correcting the stagnation pressure behind it, leading to:

$$\frac{p_2}{p_{01}} = \left(\frac{p_2}{p_{02}}\right)_i \frac{p_{02}}{p_{01}} = \left(1 + \frac{\gamma - 1}{2}\left(M_2\right)_i^2\right)^{\frac{\gamma}{1-\gamma}} k_{\text{shock}}^{\frac{1}{1-\gamma}}. \tag{2.37}$$

Figure 2.3 displays Laitone parameter for the above presented models. The intrinsic stability of the shock is ensured by the maximum at $M = \sqrt{(\gamma + 3)/2}$, provided by a jump satisfying the R-H condition.

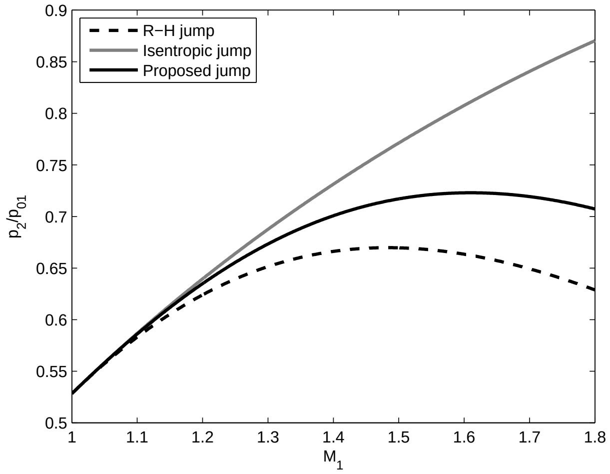

Figure 2.3: Laitone's parameter for $\gamma = 1.4$

Such a limiting behavior is completely missed in the isentropic shock model at varying Mach number, a circumstance claimed [43] as a possible explanation for the existence of multiple solutions for an FP model at transonic conditions. The parameter points out the importance of the downstream pressure field in controlling shock position and strength. It will be seen that the proposed hybridized correction leads to a significant stabilization improvement, even if the maximum value for the Laitone parameter is different and reached at a different upstream Mach condition with respect to a R-H shock.

2.2 External Boundary Conditions

The present work is focused on *external problems* typical of aeronautical applications. Such problems are analytically defined on an unbounded domain. In view of a numerical solution an external fictitious boundary must be applied to the domain, making viable numerical solutions related to some kind of numerical wind tunnel. This new boundary needs special conditions to grant the proper influence of the asymptotic condition. A non reflecting boundary is here realized by mean of characteristic variables [44]. For hyperbolic equations, like those of an unsteady potential flow, the number of physical variables that can be imposed on the external far-field boundary is related to the propagation properties of the system perturbations. The characteristic theory [32] state that the number of boundary conditions must be equal to the number of the characteristic variables related to the incoming waves. These conditions can prevent the reflection of the internal waves on the external boundary. The monodimensional non-reflecting condition is given by:

$$w_i = (w_i)_\infty \tag{2.38}$$

where w_i are the characteristic variables related to the incoming waves and ∞ identifies their asymptotic value. Subsonic asymptotic conditions involve just one incoming characteristic and just one boundary condition. The characteristic variables for monodimensional potential equations are the so-called Riemann invariants [32]:

$$w = u \pm \frac{2c}{\gamma - 1}, \tag{2.39}$$

where c is the speed of sound which can be expressed through the Bernoulli theorem:

$$\frac{c}{c_\infty} = \sqrt{1 - \frac{\gamma - 1}{c_\infty^2}\left(\phi_t + \frac{1}{2}\left(\phi_x^2 - u_\infty^2\right)\right)}. \tag{2.40}$$

The non-reflecting condition, eq. 2.38, becomes:

$$u \pm \frac{2c}{\gamma - 1} = u_\infty \pm \frac{2c_\infty}{\gamma - 1}. \tag{2.41}$$

Eq. 2.41 needs a linearizzation to be solved. Defining the perturbed potential φ:

$$\mathbf{v} = u_\infty \mathbf{i} + \nabla\varphi \rightarrow \varphi_x = u - u_\infty, \tag{2.42}$$

eq. 2.40 becomes:

$$\frac{c}{c_\infty} = 1 - \frac{\gamma - 1}{2c_\infty^2}\left(\varphi_t + \frac{1}{2}\left((u_\infty + \varphi_x)^2 - u_\infty^2\right)\right) \simeq 1 - \frac{\gamma - 1}{2c_\infty^2}\left(\varphi_t + u_\infty \varphi_x\right). \tag{2.43}$$

Combining eq. 2.43 with eq. 2.41 we obtain:

$$\varphi_x = \pm\frac{1}{c_\infty}\left(\varphi_t + u_\infty\varphi_x\right) \rightarrow \varphi_x = \pm\frac{\varphi_t}{c_\infty \mp u_\infty}. \tag{2.44}$$

Using eq. 2.42 the far-field normal inflow is obtained:

$$u = u_\infty \pm \frac{\varphi_t}{c_\infty \mp u_\infty}. \tag{2.45}$$

For a multi-dimensional domain the non reflecting condition, eq. 2.45, becomes:

$$\frac{\partial \phi}{\partial n} = V_\infty^n \pm \frac{\phi_t}{c_\infty \mp V_\infty^n}, \tag{2.46}$$

where V_∞^n is the normal component of the asymptotic speed on the boundary. This technique leads to a non reflecting condition that is exact for one dimensional cases only but remains an acceptable approximation for multi-dimensional cases, when applied normally to the boundary.

2.3 Boundary Conditions on the Body

The tangential flow condition on the body surface,

$$V_{\text{relative}}^n = V_{\text{flow}}^n - V_{\text{body}}^n = \frac{\partial \phi}{\partial n} - (\vec{V}_G \cdot \vec{n})_{\text{body}} = 0, \tag{2.47}$$

where V_{body}^n is related to body motions, states the impenetrability of the solid boundary. Evaluating on the body boundary Γ_b the last term of the integral continuity equation, eq. 2.6, and applying the boundary condition, eq. 2.47, a density flux appears at the boundary,

$$F_{body} = \int_{\Gamma_b} \rho \vec{V}_G \cdot \vec{n} d\Gamma_b. \tag{2.48}$$

On the other side, the boundary condition, eq. 2.47, has no effect on the proposed ALE integral form of the Bernoulli theorem, eq. 2.13, because no boundary integral appears.

A rigorous treatment of unsteady conditions needs a moving domain and so an ALE formulation. However, at each time step, the grid must de deformed on the fluid domain and the associated grid velocity $\vec{V}_G$ must be computed. So, the ALE formulation can involve undue computational effort in some applications. For example, when the stability of a system around a reference configuration, *i.e.* the linearized flutter, must be analyzed only small boundary motions can be considered. This allows to use *transpiration*: the domain is locked and the body motion is simulated by assigning the corresponding normal speed at the boundary. Thus, the grid velocity $\vec{V}_G$ can be neglected in the whole domain except at the solid boundary where the flux term, eq. 2.48, persists.

The transpiration was first developed by Lighthill [45]. He used a method of equivalent sources to simulate changes in airfoil thickness. Instead of thickening the actual airfoil, an equivalent surface distribution of sources is used to simulate the boundary layer. Such an approach has proven to be an effective tool for reducing the time required for unsteady aerodynamic calculations. A rigorous mathematical justification of the transpiration can be adduced by writing the fluid problem in variational form on the present configuration [46]. However, a merely qualitative explanation is here proposed. Looking at the continuity equation, eq. 2.6, and the integral Bernoulli theorem, eq. 2.13, the transpiration leads to neglect the volume terms related to the gradient of the density and the velocity potential. Actually, such terms rapidly decrease away from the body, proving the effectiveness of the transpiration technique.

Chapter 3

Numerical Solution

3.1 Unstructured Finite Volumes

In order to avoid any numerical complication related to the domain movement the proposed ALE formulation, in the form of eq. 2.6 and eq. 2.13, is implemented. As said, such a formulation is independent from the divergence of the velocity field of the domain so avoiding the need of monitoring the time derivative of the control volumes thus making it easier the choice of the transient integrator along with the interface to structural motions. Therefore, on a moving domain, the weak form of the continuity equation, eq. 2.29, and Bernoulli theorem, eq. 2.30, become:

$$\int_{\Omega}\left(\frac{d\rho}{dt}-\nabla\rho\cdot\vec{V}_G\right)d\Omega+\oint_{\Sigma}\rho\nabla\varphi\cdot\vec{n}d\Sigma=0, \tag{3.1}$$

$$\int_{\Omega}\left(\frac{d\varphi}{dt}-\nabla\varphi\cdot\vec{V}_G+\frac{1}{2}\left|\nabla\varphi\right|^2+\frac{M_{\infty}^{-2}}{\gamma-1}\left(k\rho^{\gamma-1}-1\right)\right)d\Omega=0. \tag{3.2}$$

These integral equations are treated trough a node based|centered finite volume discretization in space. The finite volume approach can also be seen as a weighted residuals finite element scheme with a piecewise constant weighting for each computational cell, combined with an integration by part. Such a double face interpretation of finite volumes is trivial. It is nonetheless stressed because our presentation of per volume operations will be more akin to a finite element than a finite volume framework.

Combining eq. 3.1 and eq. 3.2 with a nodal evaluation of the entropy transport equation,

$$k_t-\nabla k\cdot\vec{V}_G+\nabla k\cdot\nabla\varphi=0, \tag{3.3}$$

and of the wake equation,

$$\Delta\varphi_t - \Delta(\nabla\varphi)\cdot\vec{V}_G + \frac{1}{2}\Delta\left|\nabla\varphi\right|^2 + \frac{M_\infty^{-2}}{\gamma-1}\Delta\left(k\rho^{\gamma-1}\right) = 0, \tag{3.4}$$

a set of first order nonlinear Ordinary Differential Equations (ODEs) in time is obtained:

$$\boldsymbol{A}\frac{\partial\boldsymbol{x}\left(t\right)}{\partial t} = \boldsymbol{f}\left(\boldsymbol{x}\left(t\right)\right), \qquad \boldsymbol{x}^T = \left\{\rho^T \quad \varphi^T \quad k^T\right\}. \tag{3.5}$$

The pressure continuity on the wake must also be applied,

$$\Delta\left(k\rho^\gamma\right) = 0. \tag{3.6}$$

The line|surface which represents the wake is part of the domain discretization and is not trimmed according the motion field. A procedure to enucleate a wake surface within a generic unstructured tetrahedral mesh will be described in a following chapter.

3.1.1 Spatial Discretization

The spatial discretization uses triangles and tetrahedrons, *i.e.* the *elements*. The approximation for ρ, φ and k is based on linear or quadratic isoparametric shape functions within each element. The solution variables are located at the *nodes*, *i.e.* element vertices and side midpoints. The domain portion related to each node is a *cell*, *i.e.* the *finite volume*. Calling L a triangle area coordinate, Figure 3.1 shows the linear shape function L_1 for a three-node two-dimensional element.

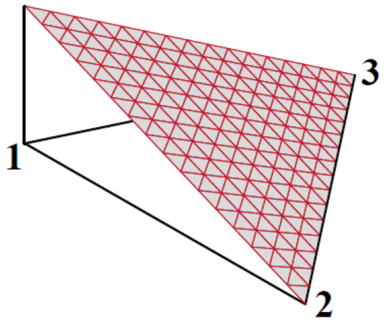

Figure 3.1: Linear shape function L_1.

The three linear shape functions are simply the triangular coordinates. The geometry of the six-node quadratic triangle is shown in Figure 3.2. Inspection reveals two types of nodes: corners (1, 2 and 3) and mid side nodes (4, 5 and 6). Consequently, we can expect two types of associated shape functions. In Figure 3.2 nodes 1 and 4 are selected as representative cases.

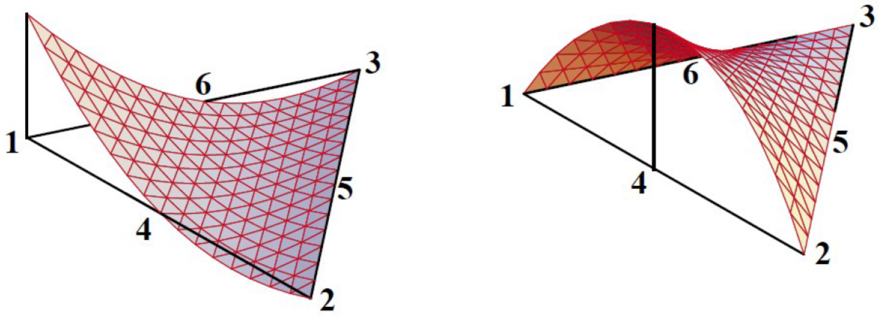

Figure 3.2: Quadratic shape functions Q_1 (left) and Q_4 (right).

For both cases quadratic shape functions Q can be produced by the product of two linear functions in the triangular coordinates:

$$Q_i = L_i(2L_i - 1) \quad \text{for} \quad i = 1, 2, 3 \ , \tag{3.7}$$

$$Q_4 = 4L_1L_2 \ , \quad Q_5 = 4L_2L_3 \ , \quad Q_6 = 4L_3L_1 \ . \tag{3.8}$$

Four-dimensional linear and quadratic shape functions for the tetrahedron cannot be properly drawn. See [47] for more details about shape functions.

3.1.2 Mesh and Elements Data Processing

The proposed formulation can be implemented in two ways. One consists of preparing cell fluxes on a per element basis, assembling nodal equations as in FEM implementations. The other one indexes elemental data globally, placing them in global sparse matrices and obtaining the equations to be solved with a few simple general sparse matrix operations. The second approach has been used here. Its efficiency relies on suitable sparse matrix manipulation libraries. The related tools are available as free(dom) software and in general Problem Solving Environments (PSEs), *e.g.* MATLAB.

The geometric treatment of the mesh concerns only its elements. Figure 3.3 shows how two-dimensional elements are handled. Four linear elements and one quadratic element are shown in order to obtain the same number of nodes for both formulations. Figure 3.4 shows the volume handling for the four-node linear tetrahedron and the ten-node quadratic tetrahedron. Triangles and tetrahedrons are divided by medians in a number of parts equal to the number of nodes. These parts build the cells.

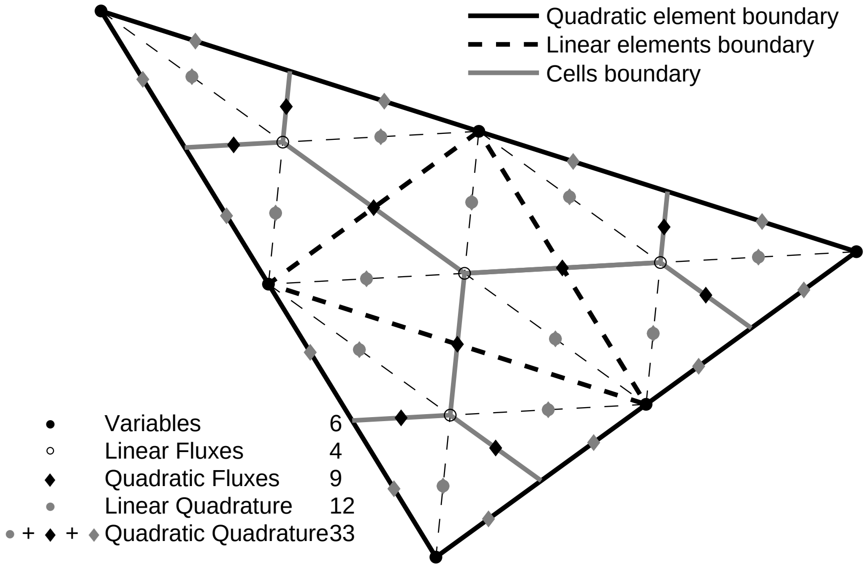

Figure 3.3: Two-dimensional elements handling

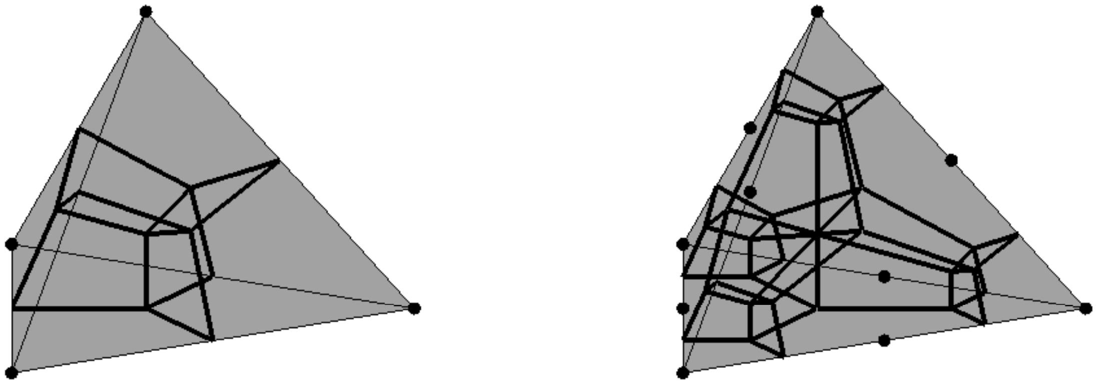

Figure 3.4: Three-dimensional elements handling

A matrix containing the vertices coordinates of the i-th element is defined:

$$M_N^i = \begin{bmatrix} x_1^i & y_1^i & \cdots & 1 \\ x_2^i & y_2^i & \cdots & 1 \\ \vdots & \vdots & \ddots & \vdots \\ x_{N+1}^i & y_{N+1}^i & \cdots & 1 \end{bmatrix}, \tag{3.9}$$

where N denotes the domain dimension (2 or 3). Then we calculate the domain portion related to each element:

$$\text{Area}|\text{Volume}_i = \left|\det\left(M_N^i\right)\right|/N! \tag{3.10}$$

The portion of domain related to each cell can be computed from the portion of domain related to each element,

$$\{Area|Volume_{cell}\}_n = \{A\}_n = [\Sigma]_{n\cdot m}\,\{1\}_m \tag{3.11}$$

where $[\Sigma]$ is a sparse matrix that computes the integral on the cells of a constant function within each element. The $\Sigma_{j,i}$ element is the portion of the i-th element related to the j-th cell. Table 3.1 collects, for the implemented elements, the weights which must multiplied with the i-th triangle area A_i or the i-th tetrahedron volume V_i to obtain the generic $\Sigma_{j,i}$ element. Quadratic elements involve different values for vertices and midpoints nodes.

	Linear	Quadratic	
		Vertices	Midp.s
Triangle	1/3	1/12	1/4
Tetrahedron	1/4	1/32	7/48

Table 3.1: Weights to build the integration matrix $[\Sigma]$

The matrix operators that allow to compute the gradient of the linear approximating shape functions are derived from the matrices previously defined, eq. 3.9. Relations between linear and quadratic shape functions, eqs. 3.7 and 3.8 for two-dimensional elements, lead to the matrix operators that allow to compute the gradient for the quadratic approximation at each h-th internal point. For the generic element we obtain:

$$\left\{\text{Grad}\,(f)_k^h\right\}_m = \left[G_k^h\right]_{m\cdot n}\{f\}_n\,, \tag{3.12}$$

where vector $\{f\}$ collects the function values at the n nodes and vector $\left\{\text{Grad}(f)_k^h\right\}$ collects the values of the k component of the function gradient at the h-th internal point whitin the m elements. The function evaluation at each h-th internal point shown in figure 3.3 is obtained from nodal values:

$$\left\{f^h\right\}_m = \left[B^h\right]_{m\cdot n}\{f\}_n\,, \tag{3.13}$$

where matrix $[B_h]_{m\cdot n}$ combines incidence and area|volume coordinates. The flux contribute at the h-th internal point can be computed,

$$\left\{F^h\right\}_m = \mathrm{diag}\left(\left[B^h\right]_{m\cdot n}\{\rho\}_n\right)\sum_k \mathrm{diag}\left(\left[G_k^h\right]_{m\cdot n}\{\varphi\}_n\right)\left\{n_k^h\right\}_m, \tag{3.14}$$

where vector $\left\{n_k^h\right\}_m$ collects the k-th component of the integrated normal at the h-th internal point within the m elements. The flux contributes are joined on the cells with proper incidence matrices,

$$\{F\}_n = \sum_h \left[A^h\right]_{n\cdot m}\left\{F^h\right\}_m. \tag{3.15}$$

The integration on the cells of functions defined within each element is also required. This is performed by a quadrature technique. The quadrature points shown in figure 3.3 lead to an exact integration for both linear and quadratic functions. For the s-th linear element the function values at the quadrature points are related to the nodal values,

$$\left\{\bar{f}\right\}_s = \tilde{I}\,\{f\}_s\,, \tag{3.16}$$

where

$$\tilde{I}_{ij} = \begin{cases} d, & \text{if} \quad i = j \\ (1-d)/N, & \text{if} \quad i \neq j \end{cases} \tag{3.17}$$

and $d = (N+1)^{-1}\sum_{k=1}^{N+1} k^{-1}$. See [47] for details about quadrature coordinates and weights for the quadratic approximation. Combining the weighing matrix $\tilde{I}$ with the element area|volume the global integration operator can be builded,

$$\left\{\hat{f}\right\}_n = [I]_{n\cdot n}\{f\}_n\,. \tag{3.18}$$

To integrate on the cells a function known on internal points only other operators must be defined,

$$\{\hat{g}\}_n = \sum_h \left[I^h\right]_{n\cdot m}\left\{g^h\right\}_m. \tag{3.19}$$

3.2 Treatment of Supersonic Regions

The finite volume scheme implies a central discretization, so an *upwind* desymmetrization bias [32] needs to be introduced to impose spatial causality in supersonic regions. The treatment of such regions consists of the introduction of *artificial viscosity* based on modifying the density to achieve a correct domain dependence for the solution,

$$\widetilde{\rho} = \rho + \Delta\rho. \tag{3.20}$$

For both linear and quadratic formulations the amount of upwind $\Delta\rho$ must be constant within each element in order to avoid oscillations in proximity of shocks. $\Delta\rho$ can be expressed as a variation of ρ along a vector Δl,

$$\Delta\rho = \nabla\rho \cdot \Delta l. \tag{3.21}$$

The modulus of Δl is then determined by considering a characteristic length l_i for each element,

$$|\Delta l_i| \propto l_i, \tag{3.22}$$

where $l_i = \sqrt{\text{Area}_i}$ for the i-th triangle and $l_i = \sqrt[3]{\text{Volume}_i}$ for the i-th tetrahedron. Different techniques can be used to define the proportionality in eq. 3.22. A standard density upwind scheme [44] is:

$$|\Delta l_i| = \varepsilon l_i. \tag{3.23}$$

whereas ε is a unique proportionality constant defined for the whole supersonic domain. The supersonic region where the upwind must be applied needs to be determined. Within each element the velocity modulus is compared to the local critical velocity,

$$\begin{cases} |V_i| > V_i^* & \rightarrow \quad |\Delta l_i| = \varepsilon l_i \\ |V_i| < V_i^* & \rightarrow \quad |\Delta l_i| = 0 \quad . \end{cases} \tag{3.24}$$

The critical velocity V_i^* within the i-th element is:

$$V_i^* = \sqrt{\frac{2 + (\gamma - 1)\, M_\infty^2}{(\gamma + 1)\, M_\infty^2} V_\infty^2 - 2\frac{\gamma - 1}{\gamma + 1}\dot{\varphi}_i}. \tag{3.25}$$

The standard upwind scheme is widely used in the literature and provides good results. Nevertheless, it needs to be calibrated with respect to the supersonic condition and the discontinuous upwind *activation*, eq. 3.24, affects the numerical stability. The proposed modified technique removes such drawbacks.

The vector Δl in eq. 3.20 must provide a value of $\widetilde{\rho}$ internal to every nodal Mach cone. So, a geometrical interpretation of the density biasing is presented in Figure 3.5 for an equilateral triangle with area A and orientation defined by α.

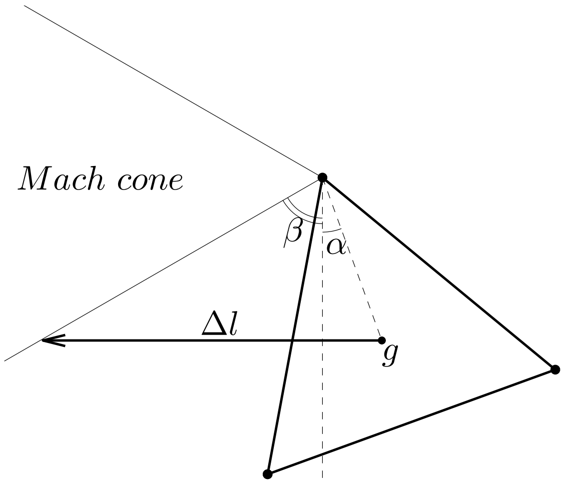

Figure 3.5: Upwind interpretation

We obtain,

$$|\Delta l| = \frac{2}{3}\sqrt[4]{3}\sqrt{A}\left(\sin\left(\alpha\right) + \cos\left(\alpha\right)\tan\left(\beta\right)\right). \tag{3.26}$$

A suitable parameter can be defined as function of the triangle orientation and the local Mach number,

$$\varepsilon\left(\alpha, M\right) = \frac{|\Delta l|}{\sqrt{A}\sqrt{M^2-1}} = \frac{2}{3}\sqrt[4]{3}\left(\frac{\sin\left(\alpha\right)}{\sqrt{M^2-1}} + \cos\left(\alpha\right)\right). \tag{3.27}$$

In order to realize the proper density biasing a geometrical inspection must be realized on each element. However, as shown in Figure 3.6, ε reveals a small variation for small values of α, typical of elements close to a body.

So, for not overly distorted mesh, the element orientation can be ignored and a unique value of ε can be choose. A suitable value of ε is approximately 0.9 for both 2D and 3D meshes. For 3D domains the local metric is defined through the element volumes, *i.e.* $\sqrt[3]{V}$. A definition of the vector Δl for the whole domain is obtained,

$$\Delta l = -\varepsilon \sqrt[2|3]{A|V}\,\Re\left(\sqrt{M^2-1}\right)\frac{\nabla\varphi}{|\nabla\varphi|}. \tag{3.28}$$

A continuous upwind *activation*, which contributes to numerical stability, is also obtained. The density variations within the m elements, collected in the

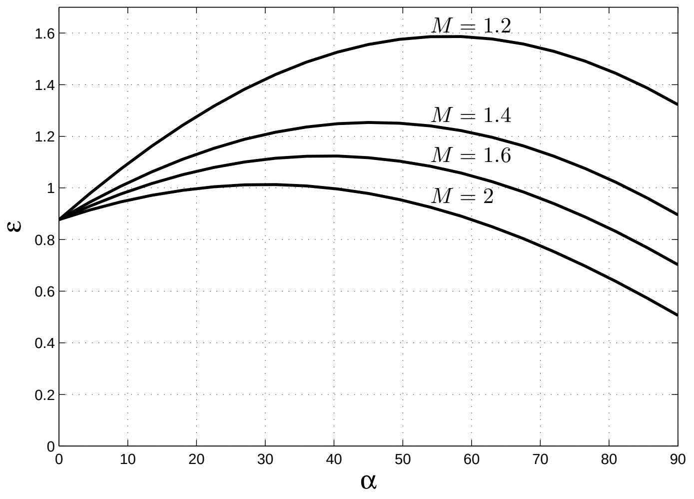

Figure 3.6: 2D upwind parameter

vector $\{\Delta\rho\}$, after applying eq. 3.28, is

$$\{\Delta\rho\} = \operatorname{diag}\left\{\frac{|\Delta l|}{|V|}\right\} \sum_k \left(\operatorname{diag}\left([G_k]\{\varphi\}\right)[G_k]\right)\{\rho\} = [U]\{\rho\}\,. \tag{3.29}$$

3.3 Weak Equations

Using the matrices presented in the previous paragraphs the discretized overall mass conservation, eq. 3.1, becomes:

$$[I]\left\{\frac{d\rho}{dt}\right\} = \{F\} + \{A\}\,, \tag{3.30}$$

where matrix $[I]$ integrates the ρ derivative on the cells from the nodal values, vector $\{F\}$ collects the cells fluxes, eq. 3.15, and

$$\{A\} = \sum_h \left[I^h\right] \sum_k \operatorname{diag}\left(\left[G_k^h\right]\{\rho\}\right)\left\{V_{G,k}^h\right\}. \tag{3.31}$$

The discrete form of Bernoulli equation in weak form, eq. 3.2, is:

$$[I]\left\{\frac{d\varphi}{dt}\right\} = \{B\} + \{C\}\,, \tag{3.32}$$

where matrix $[I]$ integrates the derivative of φ on the cells from the nodal values,

$$\{B\} = \sum_h \left[I^h\right] \sum_k \left(\operatorname{diag}\left(\left[G_k^h\right]\{\varphi\}\right)\left\{V_{G,k}^h\right\} - \frac{1}{2}\left\{|\nabla\varphi|^2\right\}\right) \tag{3.33}$$

and

$$\{C\} = \{1\} - \frac{M_\infty^{-2}}{\gamma - 1}[I]\operatorname{diag}\{k\}\left\{\rho^{\gamma-1}\right\}. \tag{3.34}$$

3.4 Wake Equations

Figure 3.7 illustrates a trailing edge and few wake nodes.

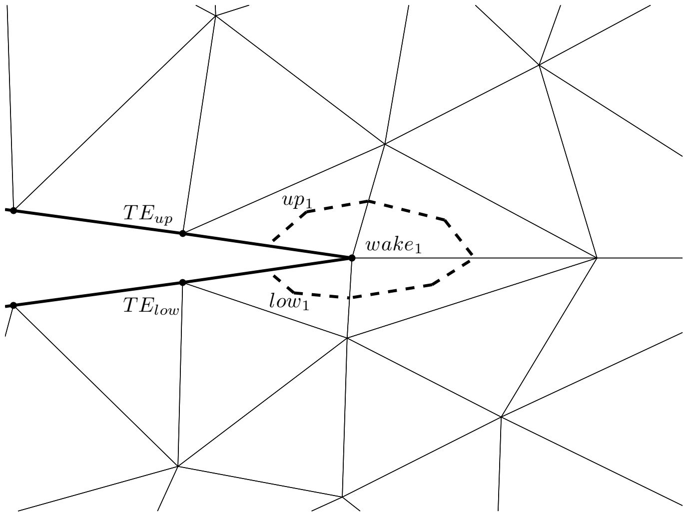

Figure 3.7: Trailing edge mesh detail

As said, the wake is a discontinuity for the functions ρ, φ and k, so it must be considered as two adjacent lines|surfaces. Two values value of ρ, φ and k are assigned to each wake node but only one control volume is defined for the discrete continuity equation, eq. 3.30, and the discrete Bernoulli theorem, eq. 3.32. The wake discontinuity adds to each function as many unknown terms as the wake nodes, so the wake conditions and the entropy transport equation restore the balance between equations and unknowns. These equations are strongly imposed on the nodal values to ensure the proper discontinuous behavior of the solution.

The pressure continuity condition on the wake, eq. 3.6, becomes

$$\operatorname{diag}\{k\}_{\mathrm{up}}\{\rho^{\gamma}\}_{\mathrm{up}} = \operatorname{diag}\{k\}_{\mathrm{low}}\{\rho^{\gamma}\}_{\mathrm{low}}\,. \tag{3.35}$$

The convective wake equation, eq. 3.4, can be discretize as:

$$\left\{\frac{d\varphi}{dt}\right\}_{\mathrm{up}} - \left\{\frac{d\varphi}{dt}\right\}_{\mathrm{low}} = \{D\} + \{E\}\,, \tag{3.36}$$

with

$$\begin{aligned}\{D\} =& \sum_k \left(\operatorname{diag}\{\varphi_{/k}\}_{\mathrm{up}}\{V_{G,k}\}_{\mathrm{up}} - \operatorname{diag}\{\varphi_{/k}\}_{\mathrm{low}}\{V_{G,k}\}_{\mathrm{low}}\right) + \\ & \frac{1}{2}\sum_k \left(\operatorname{diag}\{\varphi_{/k}\}_{\mathrm{low}}\{\varphi_{/k}\}_{\mathrm{low}} - \operatorname{diag}\{\varphi_{/k}\}_{\mathrm{up}}\{\varphi_{/k}\}_{\mathrm{up}}\right)\end{aligned} \tag{3.37}$$

and

$$\{E\} = \frac{M_{\infty}^{-2}}{\gamma - 1}\left(\operatorname{diag}\{k\}_{\mathrm{low}}\{\rho^{\gamma-1}\}_{\mathrm{low}} - \operatorname{diag}\{k\}_{\mathrm{up}}\ \{\rho^{\gamma-1}\}_{\mathrm{up}}\right). \tag{3.38}$$

The discretization of the entropy transport equation, eq. 3.3, requires some clarifications. The entropy function is assumed unknown within a layer adjacent the body-wake surface, being equal to its asymptotic value elsewhere. Defining the entropy layer as a layer of elements adjacent the surface, the entropy function is then approximated with its values at the body-wake surface only and assumed to be linearly decreasing to zero at the other layer boundary. So, the added number of unknowns with respect to an isentropic formulation is equal to the number of nodes on the body-wake surface. Numerical results carried out for meshes with different spatial discretizations justify the above approximation giving the merit of the correction to the non isentropic wake equation, eq. 3.4. So, the discrete form of the entropy equation on the body-wake surface (bw) is,

$$\left\{\frac{dk}{dt}\right\}_{bw} = \sum_k \operatorname{diag}\{k_{/k}\}_{bw}\left(\{V_{G,k}\}_{bw} - \{\varphi_{/k}\}_{bw}\right) = \{H\}\,. \tag{3.39}$$

Eq. 3.36 and eq. 3.39, because of their convective nature, are stably solved through a simple nodal collocation respecting the flow causality by evaluating the needed space gradients within the closer local upstream finite volume element. However, accepting the approximated assumption that streamlines are almost aligned with the asymptotic flow, a unique upstream element can be easily associated to each node, a priori once and for all. So, eqs. 3.3

and 3.4 are approximated though a pointwise collocation at each node with gradient computed within the associated connected upstream element. The i-th wake node must be related to one element for each wake side: up_i and low_i (Fig. 3.7). The elements up_i and low_i are the upstream elements related to the i-th node respectively above and below the wake.

The above approximations lead to a $(N-1)$D discretized entropy equations for ND domains, making the computational effort due to the entropy correction substantially negligible.

3.5 Boundary Conditions

3.5.1 Far Field Boundary

Recalling the multi-dimensional non reflecting condition, eq. 2.46, a domain with an asymptotic flow in the x direction is considered. Vector $\{n_x\}_{\text{ext}}$ collects the x component of the integrated normals of the far field surface at the external nodes and $\{|n|\}_{\text{ext}}$ collects the magnitudes of the integrated normals. The normal velocity at boundary nodes becomes:

$$\left\{\frac{\partial\varphi}{\partial n}\right\}_{\text{ext}} = \frac{\{n_x\}_{\text{ext}}}{\{|n|\}_{\text{ext}}} + \operatorname{diag}\left\{\frac{\partial\varphi}{\partial t}\right\}_{\text{ext}} \frac{\operatorname{sign}\left(\{n_x\}_{\text{ext}}\right)}{\left\{\frac{1}{M_\infty}\right\} - \frac{\{n_x\}_{\text{ext}}}{\{|n|\}_{\text{ext}}}}, \tag{3.40}$$

where divisions must be considered as element-by-element divisions. A density flux appears at the boundary,

$$\{\Delta F\}_{\text{ext}} = \operatorname{diag}\{\rho\}_{\text{ext}} \operatorname{diag}\left\{\frac{\partial\varphi}{\partial n}\right\}_{\text{ext}} \{|n|\}_{\text{ext}}\,. \tag{3.41}$$

3.5.2 Solid Boundary

As said, both the proposed ALE formulation of the continuity equation, eq. 3.1, and the transpiration, needed to deal with unsteady conditions on fixed grids, lead to a density flux at the solid boundary nodes,

$$\{\Delta F\}_{\text{body}} = \operatorname{diag}\{\rho\}_{\text{body}} \operatorname{diag}\{V_n\}_{\text{body}} \{|n|\}_{\text{body}}\,, \tag{3.42}$$

where the vector $\{V_n\}_{\text{body}}$ is related to body motions, and vector $\{|n|\}_{\text{body}}$ collects the magnitudes of the integrated normals of the solid surface at the boundary nodes.

3.6 Implicit Scheme

Eqs. 3.30, 3.32, 3.36 and 3.39 constitute a set of nonlinear ordinary differential equations in semi-explicit form. Time marching solutions can be obtained either with explicit or first|second order implicit integration schemes. Only implicit solutions are considered in this work because they can use far larger time steps than their explicit counterparts. This allows to obtain a good solution efficiency, without multigrid schemes.

In order to unify the solution procedure steady analyses are treated with fictitious transients. The *backward Euler* method is usually the most used for them because it is the simplest and there is no need for transient precision. Moreover, its high numerical dissipation (strong L-stability) accelerates the convergence to a steady state.

On the contrary, a more accurate second order scheme is used for unsteady solutions. The second order accurate implicit method is a two-step implicit scheme with controlled dissipation [48]. It can be written as:

$$x^{n+1} = a_0 x^n + a_{-1} x^{n-1} + \Delta t \left(b_1 \dot{x}^{n+1} + b_0 \dot{x}^n + b_{-1} \dot{x}^{n-1} \right) , \tag{3.43}$$

with:

$$a_0 = 1 - \beta \ , \quad a_{-1} = \beta \ , \quad b_1 = \frac{1}{2} + \delta \ , \quad b_0 = \frac{1+\beta}{2} - 2\delta \ , \quad b_{-1} = \frac{\beta}{2} + \delta \ .$$

The parameters β and δ can be expressed as functions of the desired asymptotic spectral radius ρ_∞:

$$\beta = \frac{4\left|\rho_\infty\right|^2 - \left(1 - \left|\rho_\infty\right|\right)^2}{4 - \left(1 - \left|\rho_\infty\right|\right)^2} \ , \quad \delta = \frac{1 - \left|\rho_\infty\right|^2}{8 - 2\left(1 - \left|\rho_\infty\right|\right)^2} \ .$$

The linear stability properties of the scheme can be tuned using the parameter $|\rho_\infty|$. For $|\rho_\infty| = 0$ the method results in the L-stable two-step Backward Difference Formula (BDF2). For $|\rho_\infty| = 1$, an A-stable two-step form of *Crank-Nicolson* (CN) rule results.

A generic p-step implicit scheme can be expressed as:

$$\dot{x}^{n+1} = a\left(\Delta t\right) x^{n+1} + r\left(x^n, .., x^{n-(p-1)}, \Delta t\right) , \tag{3.44}$$

where a is a coefficient and r is a residual term related to the solution at the previous step. The implicit backward Euler scheme gives:

$$a = \frac{1}{\Delta t} \quad , \qquad r = -\frac{1}{\Delta t} x^n \ ,$$

while the proposed second-order method, eq. 3.43, results in:

$$a = \frac{1}{b_1 \Delta t} \quad , \quad r = -\frac{1}{b_1 \Delta t}\left(a_0 x^n + a_{-1} x^{n-1}\right) - \frac{1}{b_1}\left(b_0 \dot{x}^n + b_{-1}\dot{x}^{n-1}\right) \; .$$

Using eq. 3.44 in eqs. 3.30, 3.32, 3.36 and 3.39 at step $n+1$ yields:

$$[I]\left(a\,\{\rho\}^{n+1} + \{r_\rho\}^n\right) = \left\{A\left(\{\rho\}^{n+1}\right)\right\}^{n+1} + \left\{F\left(\{\rho\}^{n+1}, \{\varphi\}^{n+1}\right)\right\}^{n+1}, \tag{3.45}$$

$$[I]\left(a\,\{\varphi\}^{n+1} + \{r_\varphi\}^n\right) = \left\{B\left(\{\varphi\}^{n+1}\right)\right\}^{n+1} + \left\{C\left(\{\rho\}^{n+1}, \{k\}^{n+1}\right)\right\}^{n+1}, \tag{3.46}$$

$$[I_w]\left(a\,\{\varphi\}^{n+1} + \{r_\varphi\}^n\right) = \left\{D\left(\{\varphi\}^{n+1}\right)\right\}^{n+1} + \left\{E\left(\{\rho\}^{n+1}, \{k\}^{n+1}\right)\right\}^{n+1}, \tag{3.47}$$

$$[I_k]\left(a\,\{k\}^{n+1} + \{r_k\}^n\right) = \left\{H\left(\{\varphi\}^{n+1}, \{k\}^{n+1}\right)\right\}^{n+1}. \tag{3.48}$$

$[I_w]$ is a boolean incidence matrix that computes the jump of φ at the wake and $[I_k]$ is a boolean incidence matrix which select body-wake nodal value.

Eqs. 3.45-3.48 yield a nonlinear system of equations, $\mathbf{f}\left(\mathbf{x}^{n+1}\right) = 0$, which can be solved with *Newton-Raphson* method,

$$\mathbf{f}\left(\mathbf{x}_k^{n+1}\right) + \left(\frac{\partial \mathbf{f}}{\partial \mathbf{x}}\right)_{\mathbf{x}=\mathbf{x}_k^{n+1}}\left(\mathbf{x}_{k+1}^{n+1} - \mathbf{x}_k^{n+1}\right) = 0, \tag{3.49}$$

where $\mathbf{x}_k^{n+1}$ is the solution at the previous iteration and $\frac{\partial \mathbf{f}}{\partial \mathbf{x}}$ is the Jacobian matrix of the problem. To advance the solution, an initial prediction at time step $n+1$ is needed. Either the solution at the previous step or a suitable extrapolation can be used. The latter option is followed in this work, using a cubic interpolation of the solution at two previous steps,

$$\dot{x}^{n+1} = -\frac{12}{\Delta t}x^n + \frac{12}{\Delta t}x^{n-1} + 8\dot{x}^n + 5\dot{x}^{n-1}. \tag{3.50}$$

The terms at the right-hand side of eqs. 3.45-3.48 need to be linearized. The generic flux term in the mass conservation equation, eq. 3.45, yields:

$$F^{n+1} = \oint_\Sigma \rho^{n+1}\nabla\varphi^{n+1}\cdot n d\Sigma = \oint_\Sigma \left(\rho^{n+1} + \Delta\rho^{n+1}\right)\nabla\left(\varphi^{n+1} + \Delta\varphi^{n+1}\right)\cdot n d\Sigma. \tag{3.51}$$

Neglecting the second-order term, the flux at step $n+1$ is:

$$F^{n+1} = \oint_\Sigma \rho^{n+1}\nabla\varphi^{n+1}\cdot n d\Sigma. \tag{3.52}$$

An increment flux in ρ is:

$$\Delta F_{\rho}^{n+1} = \oint_{\Sigma} \Delta\rho^{n+1} \nabla\varphi^{n+1} \cdot n d\Sigma, \tag{3.53}$$

while an increment flux in φ is:

$$\Delta F_{\varphi}^{n+1} = \oint_{\Sigma} \rho^{n+1} \nabla \left(\Delta\varphi^{n+1}\right) \cdot n d\Sigma. \tag{3.54}$$

The vector of the fluxes can be expressed as:

$$\{F\}^{n+1} = \{F\}^{n+1} + [F_{\rho}]^{n+1} \{\Delta\rho\}^{n+1} + [F_{\varphi}]^{n+1} \{\Delta\varphi\}^{n+1}. \tag{3.55}$$

The Jacobian matrices $[F_{\rho}]$ and $[F_{\varphi}]$ can be calculated by writing the flux expression in different ways. The Jacobian matrix related to ρ is obtained by writing the flux as a product by ρ. After defining the matrices:

$$\left[f^h\right] = \sum_k \left(\operatorname{diag}\left\{n_k^h\right\}\left[G_k^h\right]\right), \tag{3.56}$$

the fluxes vector becomes:

$$\{F\} = \sum_h \left(\left[A^h\right] \operatorname{diag}\left(\left[f^h\right]\{\varphi\}\right)\left(\left[B^h\right] + [U]\right)\right)\{\rho\} = [F_{\rho}]\{\rho\}. \tag{3.57}$$

The same vector can be expressed as a product by φ:

$$\{F\} = \sum_h \left(\left[A^h\right] \operatorname{diag}\left(\left(\left[B^h\right] + [U]\right)\{\rho\}\right)\left[f^h\right]\right)\{\varphi\} = [F_{\varphi}]\{\varphi\}. \tag{3.58}$$

Similar considerations can be applied to precisely compute all the not null Jacobian matrices:

$$[A_{\rho}] = \sum_h \left[I^h\right] \sum_k \operatorname{diag}\left\{V_{G,k}^h\right\}\left[G_k^h\right], \tag{3.59}$$

$$[B_{\varphi}] = \sum_h \left[I^h\right] \sum_k \operatorname{diag}\left(\left\{V_{G,k}^h\right\} - \left[G_k^h\right]\{\varphi\}\right)\left[G_k^h\right], \tag{3.60}$$

$$[C_{\rho}] = -M_{\infty}^{-2} \operatorname{diag}\{k\} \operatorname{diag}\left\{\rho^{\gamma-2}\right\}[I], \tag{3.61}$$

$$[C_k] = -\frac{M_{\infty}^{-2}}{\gamma-1} \operatorname{diag}\left\{\rho^{\gamma-1}\right\}[I], \tag{3.62}$$

$$\begin{aligned}[D_\varphi] =& \sum_k \operatorname{diag}\left(\{V_{G,k}\}_{up} - [G_k]_{up}\{\varphi\}\right)[G_k]_{up} - \\ & \sum_k \operatorname{diag}\left(\{V_{G,k}\}_{low} - [G_k]_{low}\{\varphi\}\right)[G_k]_{low}\,, \end{aligned} \tag{3.63}$$

$$\begin{aligned}[E_\rho] =& M_\infty^{-2}\operatorname{diag}\{k\}_{\mathrm{low}}\operatorname{diag}\left\{\rho^{\gamma-2}\right\}_{\mathrm{low}}[I_{low}] - \\ & M_\infty^{-2}\operatorname{diag}\{k\}_{\mathrm{up}}\operatorname{diag}\left\{\rho^{\gamma-2}\right\}_{\mathrm{up}}[I_{up}]\,, \end{aligned} \tag{3.64}$$

$$[E_k] = \frac{M_\infty^{-2}}{\gamma-1}\left(\operatorname{diag}\left\{\rho^{\gamma-1}\right\}_{\mathrm{low}}[I_{low}] - \operatorname{diag}\left\{\rho^{\gamma-1}\right\}_{\mathrm{up}}[I_{low}]\right), \tag{3.65}$$

$$[H_\varphi] = -\sum_k \operatorname{diag}\left([G_k]_{bw}\{k\}\right)[G_k]_{bw}\,, \tag{3.66}$$

$$[H_k] = \sum_k \operatorname{diag}\left(\{V_{G,k}\}_{bw} - [G_k]_{bw}\{\varphi\}\right)[G_k]_{bw}\,. \tag{3.67}$$

$[G_k]_{\mathrm{up}}$, $[G_k]_{\mathrm{low}}$ and $[G_k]_{\mathrm{bw}}$ are sub-matrices of the gradient operator $[G_k]$ which select proper upstream elements.

The global solution, residual and function vectors are defined as:

$$\{x\} = \left\{\begin{array}{c}\{\rho\}\\ \{\varphi\}\\ \{k\}\end{array}\right\}\,,\qquad \{r_x\} = \left\{\begin{array}{c}\{r_\rho\}\\ \{r_\varphi\}\\ \{r_k\}\end{array}\right\}\,,\qquad \{f_x\} = \left\{\begin{array}{c}\{A\}+\{F\}\\ \{B\}+\{C\}\\ \{D\}+\{E\}\\ \{H\}\end{array}\right\}.$$

The global integration and Jacobian matrices are:

$$[I_x] = \left[\begin{array}{ccc}[I] & [0] & [0]\\ [0] & [I] & [0]\\ [0] & [I_w] & [0]\\ [0] & [0] & [I_k]\end{array}\right]\,,\qquad [J_x] = \left[\begin{array}{ccc}[A_\rho]+[F_\rho] & [F_\varphi] & [0]\\ [C_\rho] & [B_\varphi] & [C_k]\\ [E_\rho] & [D_\varphi] & [E_k]\\ [0] & [H_\varphi] & [H_k]\end{array}\right].$$

The solution $\{x\}$ and the function $\{f\}$ at iteration $k+1$ of step $n+1$ are:

$$\{x\}_{k+1}^{n+1} = \{x\}_k^{n+1} + \{\Delta x\}_{k+1}^{n+1}\,, \tag{3.68}$$

$$\{f_x\}_{k+1}^{n+1} = \{f_x\}_k^{n+1} + [J_x]_k^{n+1}\{\Delta x\}_{k+1}^{n+1}\,. \tag{3.69}$$

The application of the integration scheme, eq. 3.44, yields:

$$\left(a\,[I_x] - [J_x]_k^{n+1}\right)\{\Delta x\}_{k+1}^{n+1} = \{f_x\}_k^{n+1} - \{r_x\}^n - a\,[I_x]\,\{x\}_k^{n+1}\,. \tag{3.70}$$

The algebraic pressure continuity condition on the wake, eq. 3.35, must be expressed in terms of $\{\Delta x\}$,

$$\begin{aligned}&\frac{1}{\gamma}\mathrm{diag}\,\{k\}_{\mathrm{up}}\;\mathrm{diag}\left\{\rho^{\gamma-1}\right\}_{\mathrm{up}}\;\{\Delta\rho\}_{\mathrm{up}}\;+\mathrm{diag}\,\{\rho^{\gamma}\}_{\mathrm{up}}\;\{\Delta k\}_{\mathrm{up}}\;=\\&\frac{1}{\gamma}\mathrm{diag}\,\{k\}_{\mathrm{low}}\,\mathrm{diag}\left\{\rho^{\gamma-1}\right\}_{\mathrm{low}}\{\Delta\rho\}_{\mathrm{low}}+\mathrm{diag}\,\{\rho^{\gamma}\}_{\mathrm{low}}\{\Delta k\}_{\mathrm{low}}\;,\end{aligned}\tag{3.71}$$

and appended to the system 3.70 to obtain the solution vector for the $(k{+}1)$th iteration. We iterate a fixed number of times or until:

$$\left\|\left\{\frac{\Delta\rho}{\rho}\right\}^{n+1}_{k+1}\right\|_{\infty} > \mathrm{tol.}\tag{3.72}$$

It can be seen that the number of per time step operations required by the implicit scheme far exceeds that of an explicit scheme. Nonetheless it surpasses a trivial implementation of its explicit counterpart because of the possibility of using far larger time steps. It is here speculated that it can remain competitive even against a multi grids based explicit implementation, because the Jacobian calculation illustrated above is simpler than multi grids iterations on unstructured meshes. Such a speculation should deserve a verification nonetheless.

A Laplace transform of the ODEs system, eq. 3.5, and the linearization around a steady state through exact Jacobian matrices, such as those used in eqs. 3.57-3.67, lead to a set of linear algebraic equations,

$$\left(\boldsymbol{J}-s\boldsymbol{A}\right)\boldsymbol{x}=\boldsymbol{F},\tag{3.73}$$

where the flux term $\boldsymbol{F}$ is related to the linearized unsteady conditions as well, *e.g.* as given by a linearized transpiration. In fact, in the linearization framework, the transpiration on the solid surface, eq. 3.42, can be seen as the sum of a geometric and a kinematic contribution. In the Laplace domain becomes:

$$\boldsymbol{F}=\left(\boldsymbol{P}+s\boldsymbol{R}\right)\boldsymbol{q},\tag{3.74}$$

where the vector $\boldsymbol{q}$ collects the generalized displacements. Eq. 3.73 leads to the solution,

$$\left(\boldsymbol{J}-s\boldsymbol{A}\right)\boldsymbol{x}=\left(\boldsymbol{P}+s\boldsymbol{R}\right)\boldsymbol{q}.\tag{3.75}$$

Computing the aerodynamic force acting on the body and projecting them on the space of the generalized displacements we obtain the linearized generalized forces in the complex domain,

$$\boldsymbol{Q}=q_{\infty}\boldsymbol{H_{am}}(s,M_{\infty})\boldsymbol{q},\tag{3.76}$$

where the asymptotic dynamic pressure q_∞ and the aerodynamic transfer functions matrix $\boldsymbol{H_{am}}(s, M_\infty)$ appear. So, the stability properties of the linearized system around a reference condition can be investigated directly in the frequency domain in a Generalized Aeroelastic Analysis Method (GAAM) way [49],

$$\left(s^2\boldsymbol{M} + s\boldsymbol{C} + \boldsymbol{K} - q_\infty \boldsymbol{H_{am}}(s, M_\infty)\right)\boldsymbol{q} = 0, \tag{3.77}$$

where $\boldsymbol{M}$, $\boldsymbol{C}$ and $\boldsymbol{K}$ are the usual generalized structural matrices. Such a problem admits nontrivial solutions if the matrix $\boldsymbol{S}(s, V_\infty)$ is singular and is closed in the complex unknown s setting the velocity V_∞. However, the aerodynamic transfer functions matrix $\boldsymbol{H_{am}}(s, M_\infty)$ is usually determined for a limited set of discrete values of s and M_∞ and, generally, for purely harmonic boundary conditions only, *i.e.* with $s = j\omega$. The only analytical closed form for aerodynamic transfer functions is related to a 2D airfoil in an incompressible flow. Such a case involves the Theodorsen function [50] which can be utilized in tabulated form for a series of reduced frequencies or in approximate forms. The generalized Theodorsen function can also be used [49]. It involves the modified Bessel functions defined in the s-plane.

Anyway, the stabilty matrix $\boldsymbol{S}(s, V_\infty)$ has non constant complex elements. Thus, common eigenvalue methods cannot be applied to solve the coupled problem, eq. 3.77. *Ad hoc* methods, such as the *p-k* method [51], must be used. The problem can also be seen as a linear homogeneous system in $\boldsymbol{q}$ and nonlinear in s. It can be solved in an iterative way by adding a generic normalization rule for the vector $\boldsymbol{q}$ and setting the velocity V_∞ [52, 53].

An alternative approach uses the theory of dynamic systems to predict aeroelastic instabilities of the Hopf type, which commonly leads to flutter or Limit–Cycle Oscillation (LCO). An Hopf bifurcation with respect to a parameter occurs when a pair of complex conjugate eigenvalues of the system Jacobian matrix related to an equilibrium condition crossing the imaginary axis. Recent applications use a Schur complement eigenvalue formulation [35]. This approach views the coupled aeroelastic system as a modified structural eigenvalue problem corrected with the aerodynamic interaction.

All of the above discussed procedures require a precise evaluation of the aerodynamic Jacobian matrix, and eventually repeated solutions, at each desired steady state, *i.e.* flight condition. These operations can affect the feasibility of such procedures. On the contrary, as will be seen, time marching simulations can be carried out with ficticious Jacobian matrices, making it possible the simulation of different conditions with a reduced factorization cost. For these reasons aeroelastic stability properties will be evaluated characterizing the aerodynamic system with proper time marching simulations and then identifying the $\boldsymbol{H_{am}}$ matrix to move onto the frequency domain.

3.7 Stability Analysis

A linearized stability analysis is here presented to cover transonic and supersonic asymptotic flows. The isentropic one-dimensional problem is considered,

$$\frac{\partial \rho}{\partial t}+\frac{\partial}{\partial x}\left(\left(\rho-u\frac{\partial \rho}{\partial x}h\right)\frac{\partial \varphi}{\partial x}\right)=0, \tag{3.78}$$

$$\frac{\partial \varphi}{\partial t}+\frac{1}{2}\left(\left(\frac{\partial \varphi}{\partial x}\right)^2-1\right)+\frac{M_\infty^{-2}}{\gamma-1}\left(\rho^{\gamma-1}-1\right)=0, \tag{3.79}$$

where $u=\Re\left(\sqrt{M_\infty^2-1}\right)$ is the upwind parameter and h defines the spatial discretization. After defining the incremented functions: $\rho=\rho_\infty+\rho$, $\varphi=\varphi_\infty+\varphi$ and setting: $\rho_\infty=V_\infty=1$, the linearized formulation can be written:

$$\frac{\partial \rho}{\partial t}+\frac{\partial \rho}{\partial x}-u\frac{\partial^2 \rho}{\partial x^2}h+\frac{\partial^2 \varphi}{\partial x^2}=0, \tag{3.80}$$

$$\frac{\partial \varphi}{\partial t}+\frac{\partial \varphi}{\partial x}+M_\infty^{-2}\rho=0. \tag{3.81}$$

A stability evaluation can be performed on the linearized formulation. For any difference scheme in the form:

$$u_j^n=\sum_{\omega=-\infty}^{\infty}\alpha_\omega e^{i\omega jh}\gamma_\omega^n,\quad j=0,\pm1,\pm2,...,\quad n\geq 1, \tag{3.82}$$

where $\gamma_\omega \in C$ is the *amplification coefficient* related to the frequency ω, a Von Neumann analysis states that the scheme is strongly stable if $|\gamma_\omega|\leq 1\ \forall\omega$. Using for simplicity a *backward centered Euler* scheme eqs. 3.80-3.81 becomes:

$$\begin{aligned}\rho_j^{n+1}=\rho_j^n-\frac{\Delta t}{h}\frac{\rho_{j+1}^{n+1}-\rho_{j-1}^{n+1}}{2}+u\frac{\Delta t}{h}\left(\rho_{j+1}^{n+1}-2\rho_j^{n+1}+\rho_{j-1}^{n+1}\right)\\ -\frac{\Delta t}{h^2}\left(\varphi_{j+1}^{n+1}-2\varphi_j^{n+1}+\varphi_{j-1}^{n+1}\right),\end{aligned} \tag{3.83}$$

$$\varphi_j^{n+1}=\varphi_j^n-\frac{\Delta t}{h}\frac{\varphi_{j+1}^{n+1}-\varphi_{j-1}^{n+1}}{2}-M_\infty^{-2}\Delta t\rho_j^{n+1}. \tag{3.84}$$

Considering: $u_{j+1}=u_je^{i\omega h}$, $u_{j-1}=u_je^{-i\omega h}$, $e^{ix}-e^{-ix}=2i\sin(x)$, $e^{ix}+e^{-ix}=2\cos(x)$, we obtain:

$$\left\{\begin{array}{c}\rho\\ \varphi\end{array}\right\}_j^n=\left[\begin{array}{cc}1+ig\sin(\omega h)+2ufg & -2fg/h\\ \Delta t/M_\infty^2 & 1+ig\sin(\omega h)\end{array}\right]\left\{\begin{array}{c}\rho\\ \varphi\end{array}\right\}_j^{n+1}, \tag{3.85}$$

where $f = 1 - \cos(\omega h)$ and $g = \Delta t/h$. The eigenvalues of the scheme result:

$$\gamma_{1,2} = \left(1 + \mathrm{CFL} \cdot M_\infty \left(uf + i\left(\sin(\omega h) \pm \sqrt{2f/M_\infty^2 - u^2 f^2}\right)\right)\right)^{-1}, \tag{3.86}$$

where $\mathrm{CFL} \cdot M_\infty = g$. Such a backward implicit Euler integration scheme is thus strongly stable for any values of ω, M_∞ and CFL making it the perfect candidate for swiftly converging steady state solutions. A similar proof is not that easy for the precise unsteady calculations required for flutter analyses, where a second order method with controllable numerical dissipation is mostly used. The linearized stability analysis of such a precise method is much more involved than the one previously presented, so its stability properties have been verified to be much the same through numerical experimentations only.

3.8 Solution Procedure

The set of first order nonlinear ODEs, eq. 3.5, leads to a set of nonlinear algebraic equations trough a time marching integration scheme. Considering once more the backward Euler scheme for simplicity, at the n_{th} integration step eq. 3.5 becomes:

$$\boldsymbol{A}\frac{\boldsymbol{x}^{n+1} - \boldsymbol{x}^n}{\Delta t} = \boldsymbol{f}\left(\boldsymbol{x}^{n+1}\right). \tag{3.87}$$

Using a Newton-Raphson (N-R) method eq. 3.87 leads to iterating the solution of the set of linear algebraic equation,

$$\boldsymbol{A}\left(\boldsymbol{x}_k^{n+1} + \Delta\boldsymbol{x}_{k+1}^{n+1} - \boldsymbol{x}_n\right) = \Delta t \boldsymbol{f}_k^{n+1} + \Delta t \boldsymbol{J}_k^{n+1} \Delta\boldsymbol{x}_{k+1}^{n+1}, \tag{3.88}$$

where the actual Jacobian matrix $\boldsymbol{J}_k^{n+1}$ appear. Rearranging eq. 3.88 one obtains:

$$\left(\boldsymbol{A} - \Delta t \boldsymbol{J}_k^{n+1}\right)\Delta\boldsymbol{x}_{k+1}^{n+1} = \boldsymbol{B}\Delta\boldsymbol{x} = \boldsymbol{b}. \tag{3.89}$$

The iterated solution of such a linear system determines most of the computational effort associated to each iteration, so that the adopted solver strategy is crucial for the obtainable computational efficiency. A GMRES method is here used to solve such a linear system. The keystone of such an iterative resolution technique is the choice of an appropriate preconditioner. In order to provide an efficient preconditioner it is possible to adopt a couple of simple approximations. At first, a zero order approximation can be used for ρ, by assuming it constant at each node, so increasing the preconditioner sparsity. Then an incomplete *LU* factorization will further enhance the sparsity of the preconditioning procedure, with a consequent overall improvement of efficiency for both the factorization and the following iterated forward-backward substitutions, made furthermore easier by the accompanying the overall reduced memory footprint. The incomplete factorization is obtained by imposing a drop tolerance to the *LU* routine provided by *UMFPACK* [54], so to result in about half of the fill-in of a complete factorization. Available incomplete factorization routines showed no competitive performances in comparison with the proposed one. A notable, though not so unexpected, discovery is that the adopted implicit integration scheme is so robust to allow to use the preconditioner for an undisturbed flow, *i.e.* a flow with uniform density and velocity, at a single Mach number, unchanged over a significant range of differing flow conditions, including: lifting, non-lifting, steady, unsteady, subsonic, transonic and supersonic solutions. Since such flow parametrized analyses are almost compulsory in any practical design activity the FP formulation here presented might prove quite efficient just because of the above preconditioning property. A slight further efficiency improvement has been achieved with a matrix-free GMRES. In such a case only one full precision evaluation of the residuals would be required for each internal iteration. The matrix-free approach also involves a slight memory saving because many of the matrices needful to compute the preconditioner can be deleted after the factorization.

A qualitative and partially quantitative explanation of the above mentioned preconditioner properties can be justified with a somewhat standard linear convergence analysis of the related iteration process. We consider the actual linear problem, eq. 3.89, related to the actual Mach number M_n of interest and denote as $\boldsymbol{B}_0$ the preconditioning matrix related to the chosen, differing, Mach number M_0. Then the $(k+1)_{th}$ step of above mentioned iteration procedure can be written as:

$$\boldsymbol{B}_0 \Delta \boldsymbol{x} = \boldsymbol{B}_0 \boldsymbol{x}_{k+1} - \boldsymbol{B}_0 \boldsymbol{x}_k = \boldsymbol{b} - \boldsymbol{B} \boldsymbol{x}_k, \tag{3.90}$$

from which:

$$\boldsymbol{x}_{k+1} = \boldsymbol{B}_0^{-1} \boldsymbol{b} + \left(\boldsymbol{I} - \boldsymbol{B}_0^{-1} \boldsymbol{B} \right) \boldsymbol{x}_k. \tag{3.91}$$

Assuming the above difference equation is asymptotically stable, it is clear that $\boldsymbol{x}_{k+1} = \boldsymbol{x}_k$ eventually. On the other hand the stability will be assured if the eigensolutions associated to its general solution, *i.e.* of $\left(\boldsymbol{I} - \boldsymbol{B}_0^{-1} \boldsymbol{B} \right)$, have eigenvalues satisfying $\max |\lambda| < 1$, the related convergence being faster and faster as $\max |\lambda| \ll 1$. Thanks to the stability analysis of the previous section a general close form verification is likely possible, just for a linear(ized) one dimensional case, for which one obtains:

$$|\lambda_{1,2}| = \left|1 - \frac{\gamma_n}{\gamma_0}\right| = \left|1 - \frac{1 + \mathrm{CFL} M_0 \left(uf + i\left(\sin(\omega h) \pm \sqrt{2f/M_0^2 - u^2 f^2}\right)\right)}{1 + \mathrm{CFL} M_n \left(uf + i\left(\sin(\omega h) \pm \sqrt{2f/M_n^2 - u^2 f^2}\right)\right)}\right|. \tag{3.92}$$

A sample of the thus obtainable analytical stability regions, shown in Figure 3.8, provide an indication of the persistence of such a single preconditioner for two fairly separated CFL values, i.e. 10 and 1000.

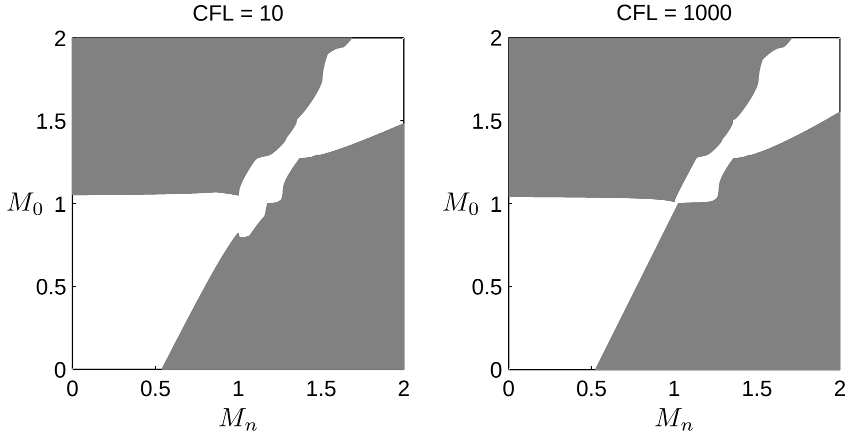

Figure 3.8: Stability regions (white) for the iterative scheme

It is finally remarked that the proof adopted for the behavior of the iterated imprecise solution is based on using an exact linear solution. Numerical verifications with the GMRES solver allows conjecturing that it can even widen the associated stability regions. Such a conjecture should be supported by noting that GMRES based iterations are somewhat similar to those of inverse power iterations. Consequently they tend to filter the high frequency content of any solution, so improving the iteration procedure to the point of making it possible the mentioned widening of the convergence regions. It should be nonetheless clear that the be usable such an approach should not require too many iterations.

The above discussed procedure works for every precisely solved flow condition but can be redundant in same cases. In such a view we distinguish between an Homogeneous Flow (HF) and an sub-supersonic Transonic Flow (TF). An HF is related either to fully subsonic or supersonic flows. The latter are typically associated to thin bodies with weak attached shocks. For TFs the use of an iterative solver is almost compulsory but for HFs a generalization of the modified N-R method can be applied to the problem using an unique tangent matrix for every time step and internal iteration. Once more the Jacobian matrix of a single unperturbed condition is used, possibly mated to an incomplete factorizations. So, denoting as $\boldsymbol{J}_0$ the Jacobian Matrix related to the unperturbed condition at a different asymptotic Mach number, M_0, eq. 3.89 becomes:

$$\left(\boldsymbol{A} - \Delta t \boldsymbol{J}_0\right) \Delta \boldsymbol{x}_{k+1}^{n+1} = \boldsymbol{B}_0 \, \Delta \boldsymbol{x} = \boldsymbol{b}, \tag{3.93}$$

where a constant matrix and the actual residual appear again. Performing a suitable incomplete factorization of the matrix, the computational cost of such an implicit iterative scheme results comparable to that of an explicit scheme because only the residual evaluation and a forward-backward solving are required. The numerical results presented in the next section prove the efficiency of such a solution procedure. The above discussed procedure can impose undue computational costs on fictitious transients toward steady state solutions, where we want to fully profit of the proven unconditional stability by using unduly large CFLs and do not care for a precise solution at the fictitious time steps, caring just of keeping it converging to steady state. In this case only one N-R iteration can be performed for any time step reducing the computational effort due to the residual evaluation. For the liner(ized) problem the linear system, eq. 3.93, becomes:

$$\boldsymbol{B}_0 \, \Delta \boldsymbol{x} = \boldsymbol{J}^n \boldsymbol{x}^n. \tag{3.94}$$

A stability analysis of such an integration scheme can be performed by rearranging eq. 3.94,

$$\boldsymbol{x}^{n+1} = \left(\boldsymbol{A} - \Delta t \boldsymbol{J}_0\right)^{-1} \left(\boldsymbol{A} - \Delta t \boldsymbol{J}_0 + \Delta t \boldsymbol{J}^n\right) \boldsymbol{x}^n, \tag{3.95}$$

and using the definition of the Jacobian matrix $\boldsymbol{J}^n$ for the one-dimensional linearized problem,

$$\Delta t \boldsymbol{J}^n = \mathrm{CFL} \cdot M_n \left[\begin{array}{cc} -i \sin(\omega h) - 2uf & 2f/h \\ -h/M_n^2 & -i \sin(\omega h) \end{array} \right]. \tag{3.96}$$

The comparison of the thus obtainable analytical stability regions of Figure 3.9, with those shown in Figure 3.8, confirms the effectiveness of such a fast integration scheme.

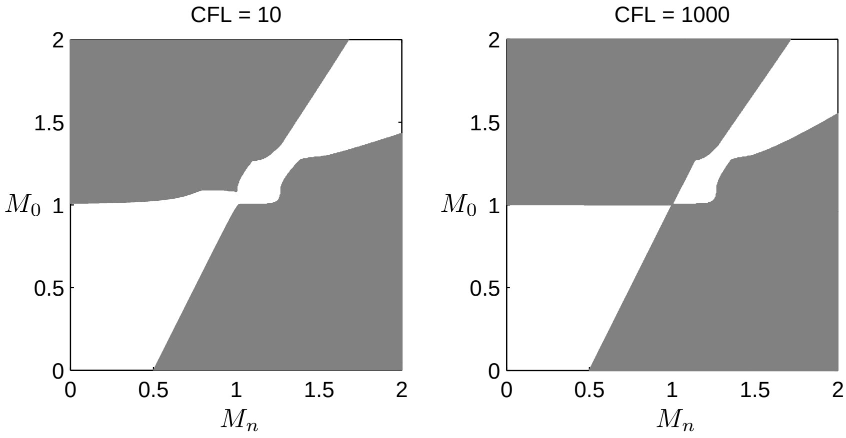

Figure 3.9: Stability regions (white) for the integration scheme

Chapter 4

Flutter Analysis

4.1 Overview

The interaction between a deformable structure and the fluid surrounding it gives rise to a rich variety of physical phenomena which may be of primary importance in many fields of engineering. Aeroelastic phenomena may be either of a dynamic nature, as flutter or buffet, or static, as divergence or control surface reversal. The first is here discussed.

In the framework of classical aeroelasticity, a flutter analysis can be carried out with the study of the stability properties of the aeroelastic system linearized around a reference condition. So, the flutter analysis concerns the study of the system eigenvalues. In particular, a flutter occurs when a structural eigenvalue reach a zero-damping condition due to the iteration with the surrounding fluid. The hypothesis of linearity (locally at least) of the aeroelastic system is crucial to reduce the computational costs. In transonic flow aerodynamic nonlinearities tend to be most important. Indeed, it is often observed that the transonic flow regime is inherently nonlinear in the governing field equations. However, at any Mach number for any airfoil, if the angle of attack is sufficiently small, the aerodynamic forces and shock motion will be linear in the angle of attack. Moreover, as the frequency of the angle of attack motion increases, the range of angle of attack over which linear behavior persists increases [55]. So, the hypothesis of local linearity can be applied to transonic conditions too. Such an hypothesis involves the need of a linear Reduced Order Model (ROM) of the aerodynamic system. Defining a generic displacement field $\boldsymbol{u}(x)$ the related generalized inviscid aerodynamic force can be expressed as

$$Q^a(t) = q_\infty \int_S C_P(x,t)\boldsymbol{u}(x) \cdot \boldsymbol{n} dS, \tag{4.1}$$

where $q_\infty C_P(x,t)$ is the aerodynamic pressure field acting on the body surface S whose orientation is locally defined by the normal $\boldsymbol{n}$. The unsteady variation of the aerodynamic loads about a reference trimmed solution due to small structural displacements is conveniently modelled, directly in the Laplace domain, by means of the aerodynamic transfer functions matrix $[H_{am}(p, M_\infty)]$. So, the vector of the generalized aerodynamic forces can be expressed as a function of the structural generalized displacements $\{q(s)\}$,

$$\{Q^a(s)\} = q_\infty \left[H_{am}(p, M_\infty)\right] \{q(s)\}\,, \tag{4.2}$$

where the dynamic pressure q_∞ and the Mach number M_∞ are related to the reference trimmed condition and the complex reduced frequency $p = sLa/V_\infty = h + jk$ depends on the reference aerodynamic length La and the flight velocity V_∞. Actually $[H_{am}(p)]$ is known only on the imaginary axis and must be suitably extrapolated on the whole complex domain.

The definition of the generalized aerodynamic forces in the Laplace domain, eq. 4.2, is not adequate to face modern aero-servo-elastic problems, such as the control system design for flutter suppression or gust loads attenuation. A suitable representation of the aerodynamic system in the time domain is required to use the modern control system design techniques. This leads to the so-called *modern* aeroelasticity [56, 57]. So, the aerodynamic transfer functions matrix $[H_{am}]$ can be used for frequency domain analysis or can be transformed in a state space time domain system using any of the techniques currently adopted. The result is a state space system which can be connected in feedback with the structural model and so used for all types of dynamic analyses and stability investigations. Such an approach is not followed in the present work and only classical aeroelasticity will be considered.

4.2 Aerodynamic Transfer Functions

The definition of the aerodynamic forces acting on the structural sub-system is crucial for aeroelastic analyses. As said, the aerodynamic transfer functions matrix $[H_{am}]$ can be evaluated directly in the Laplace domain with a proper representation of the unsteady boundary condition. However, such an approach can involve undue computational costs using nonlinear aerodynamics because a precise evaluation of the aerodynamic Jacobian matrix must be performed at each desired steady state. So, the matrix $[H_{am}]$ is here obtained with numerical time marching simulations. First, the steady solution for the aeroelastic system, *i.e.* the trimmed deformed condition representing the reference for the linearization, must be reached. Now the vector of the generalized aerodynamic forces $\{Q^a(t)\}$ due to a prescribed law of motion of the i-th generalized displacement $q^i(t)$ can be computed. The i-th column of the aerodynamic transfer functions matrix $[H_{am}(k)|i]$ is the ratio between the Fourier transform of the output and input signal of the aerodynamic system,

$$[H_{am}(k)|i] = \frac{\mathcal{F}(\{Q^a(t)\})}{\mathcal{F}(q^i(t))}, \tag{4.3}$$

where the operator $\mathcal{F}$ can be efficiently implemented by the Fast Fourier Transform (FFT) algorithm. Performing such an operation for each structural degree of freedom the whole aerodynamic transfer functions matrix $[H_{am}(k)]$ is obtained. The procedure is computationally efficient due to the use of the transpiration to impose the unsteady conditions. The linear behaviour of the nonlinear aerodynamic system around the reference state is obtained through a finite difference numerical linearization of the boundary conditions. Such a linearization splits the boundary condition in a geometric and a kinematic contribution. So, two independent identifications could be performed for such two contributions thus allowing a proper excitation for both of them. However, such an approach duplicates the computational costs and a unique excitation is usually applied. The law of motion for the i-th generalized displacement $q^i(t)$ must excite the desired reduced frequency range $[0, k_{max}]$. Moreover, the amplitude of the displacement must be large enough to overcome the numerical noise but not too large to preserve the small perturbation hypothesis. Among possible input signal the classical are: sinusoidal, impulse and step. The characterization through sinusoidal input seems the most natural but it is extremely expensive in terms of computational costs, because each degree of freedom needs to be tested for a set of imposed frequency. The other two cases, at least ideally, require just one test for each input to characterize completely the system in the whole range of frequencies of interest. The better choice seems to be a blended step input,

$$q^i(\tau) = \begin{cases} \frac{A_q}{2}\left(1 - \cos(k_q \tau)\right) & \text{if} \quad \tau < \tau_q \\ A_q & \text{if} \quad \tau \geq \tau_q, \end{cases} \tag{4.4}$$

where the nondimensional time $\tau = tV_\infty/La$ appears. The reduced frequency k_q, the nondimensional time τ_q and the amplitude A_q must be chosen to guarantee the above discussed requirements. The blended step is computationally efficient because it does not require excessive time resolution to be described, otherwise needful for an impulse, and prevents Gibbs phenomena in the transient, typical of a not blended step. To avoid the singularity related to the asymptotic value $(1/jk)$ the generic signal $z(t)$ can be expressed as a sum of the asymptotic value z_∞ and the *deficiency* function,

$$D_z(t) = z(t) - z_\infty. \tag{4.5}$$

So, the system relation, eq. 4.3, becomes,

$$[H_{am}(k)|i] = \frac{\{Q^a_\infty\} + jk\mathcal{F}(\{Q^a(t)\} - \{Q^a_\infty\})}{\{q^i_\infty\} + jk\mathcal{F}(\{q^i(t)\} - \{q^i_\infty\})}. \tag{4.6}$$

4.3 Structural Sub-System

In the framework of Ritz's numerical methods, the unknown structural displacement field $s(x,t)$ is represented as a function of a complete set of space dependent shape functions $N_i(x)$ and a set of time dependent generalized displacements $q_i(t)$,

$$s(x,t) \simeq \sum_{i=1}^{n_s} N_i(x) q_i(t) = [N(x)]\{q(t)\}. \tag{4.7}$$

Such an approach leads the structural problem to a system of ODEs,

$$[M]\{\ddot{q}(t)\} + [C]\{\dot{q}(t)\} + [K]\{q(t)\} = \{Q^a(t)\}, \tag{4.8}$$

where $[M]$, $[C]$ e $[K]$ are the generalized mass, damping and stiffness matrices. The array of the Generalized Aerodynamic Forces (GAFs) $\{Q^a(t)\}$ is assembled by projecting the aerodynamic pressure field acting on the body surface S onto the structural shape functions,

$$\{Q^a(t)\} = q_\infty \int_S C_P(x,t)[N(x)]^T \boldsymbol{n} dS. \tag{4.9}$$

To solve the structural problem the set of shape functions $N_i(x)$ and the number of structural degree of freedom n_s must be chosen. The compact-support Lagrange polynomial shape functions of the Finite Element Method (FEM) can be used. So, the generalized displacements $q_i(t)$ become the nodal displacements $\{u_s\}$. However, for such a formulation, the number of degree of freedom n_s to obtain an acceptable accuracy is generally too large. Alternatively, the set of shape functions can be obtained by means of an eigenvalues analysis of a finite element model which leads to the structural normal modes of vibrations. Moreover, such a structural model can be tuned with Ground Vibration Tests (GVTs). Because of the favourable convergence properties of such shape functions a limited number of degree of freedom is sufficient to build an accurate and efficient condensed numerical model of the structural sub-system. Moreover, the orthogonality properties of the normal modes imply that the generalized mass and stiffness matrices are diagonal. Rigid modes associated with control surfaces can also be modelled. However, normal modes cannot grant rapid convergence when concentrated loads are applied on the structure. In such conditions the modal base must be extended with proper static deformation modes. The hybrid base leads to non diagonal generalized matrices but the efficiency persists due to the small dimension of the base.

4.4 Fluid-Structure Coupling

Regardless of the nature of the treated phenomenon a fundamental ingredient of an aeroelastic analysis is the so-called aeroelastic interface. It must realize the closed-loop connection between the structural and aerodynamic sub-systems by means of a suitable interpolation strategy. The structural displacement and velocity fields must be translate into a variation of the boundary conditions on the aerodynamic sub-system and the aerodynamic forces field must become a load condition acting on the structural sub-system. The aeroelastic interface scheme can be represented by means of a linear operator $[L]$ which suitably interpolates the structural displacements $\{u_s\}$ onto the aerodynamic boundary nodes displacements $\{u_a\}$,

$$\{u_a\} = [L]\{u_s\}\,. \tag{4.10}$$

A succesfull aeroelastic interface scheme must link models with non-matching spatial domains and numerical grids and ensure the conservation of the momentum and energy exchanged between the two sub-systems. The introduction or removal of spurious energy by the interface scheme may affect the overall stability properties of the aeroelastic system. Such a property can be translate on the equivalence of the virtual work made by the aerodynamic forces $\{F^a\}$ on the two sub-systems,

$$\delta L = \delta\{u_a\}^T\{F_a^a\} = \delta\{u_s\}^T\{F_s^a\}\,. \tag{4.11}$$

Substituting eq. 4.10 in eq. 4.11 we obtain the linear operator which interpolates the aerodynamic forces from the aerodynamic to the structural system,

$$\{F_s^a\} = [L]^T\{F_a^a\}\,. \tag{4.12}$$

4.4.1 Moving Least Squares

The aeroelastic interface operator of eq.4.10 is here builded by means of an interpolation scheme based on a Moving Least Squares (MLS) technique [56, 58]. Such a scheme is able to deal with complex configurations and extremely different structural and aerodynamic meshes. A local approximation of structural displacement field must be builded by means of a sum of n polynomial basis functions,

$$\tilde{u}_s(x) = \sum_{k=1}^{n} f_k(x) a_k(x), \tag{4.13}$$

where $f_k(x)$ is the k_{th} basis function while $a_k(x)$ is the k_{th} unknown coefficient. The coefficients $a_k(x)$ are obtained by performing a weighted least square fit for the approximation:

$$\text{Minimize} \;\; J(x) = \int_\Omega W(x-\bar{x}) \left(\tilde{u}_s(x) - u_s(\bar{x})\right) d\Omega(\bar{x}). \tag{4.14}$$

The problem can be localized by choosing compact support weight functions $W(x)$ such as smooth non-negative Radial Basis Functions (RBF). The type of function and the support radius must be chosen to obtain a smooth interpolation and to cover enough structural nodes. As an example of the robustness and quality of the MLS scheme, the reconstruction onto the aerodynamic boundary mesh of a deformable modal shapes of the FE structural model of the HIRENASD wing [59] is shown in Figure 4.1.

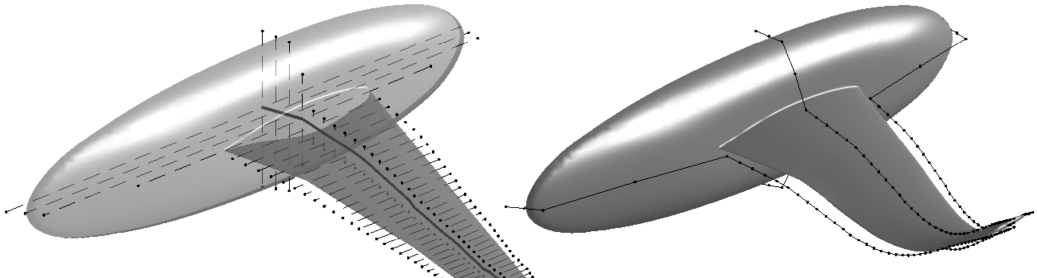

Figure 4.1: MLS interface for HIRENASD wing

The available beam model has been modified by introducing for each node a set of four nodes rigidly linked to the first one, as shown in Figure 4.1. Then, a normal modes analysis has been carried out. The first modal shape is shown in Figure 4.1. The added nodes ensure a better spatial definition of the modal displacements and a proper reconstruction onto the aerodynamic boundary mesh.

4.5 Flutter Calculation

Moving on the Laplace domain and recalling the expression of the GAFs, eq. 4.2, the structural problem, eq. 4.8, falls in the framework of classical aeroelasticity as an algebraic homogeneous system,

$$\left(s^2[M] + s[C] + [K] - q_\infty[H_{am}(p, M_\infty)]\right)\{q(s)\} = 0. \tag{4.15}$$

Such a system admits nontrivial solutions if the matrix $[A(s, V_\infty)]$ is singular and is closed in the complex unknown s setting the velocity V_∞. Starting from $V_\infty = 0$, the roots loci can be builded for the whole flight envelope. The so-called $V_\infty - \omega$ and $V_\infty - g$ diagrams, where $g = 2\sigma/\sqrt{\sigma^2 + \omega^2}$, suitably represent the stability properties of the system. The first intersection in the $V_\infty - g$ diagram with the g axis identifies the flutter velocity, *i.e* the zero-damping condition.

The most considerable difficulty in aeroelastic analyses concerns the definition of the aerodynamic transfer functions matrix $[H_{am}(p, M_\infty)]$. Usually, it is known for a set of discrete values of p and M_∞ and, generally, for purely harmonic boundary conditions only, *i.e.* with $p = ik$. Thus, common eigenvalue methods cannot be applied to solve the coupled problem, eq. 4.15, and *ad hoc* methods must be used. The most common strategy is the well-known *p-k* [51] which is based upon the assumption that the aerodynamic transfer functions matrix $[H_{am}(p)]$ computed for purely harmonic motions, *i.e.* with $p = ik$, is an acceptable approximation for slightly damped motions, *i.e.* with $p = \varepsilon + ik$ and $\varepsilon \ll 1$. However, such a method can involve some difficulties in tracking intersecting eigenvalues. The approach used in the present work and described below prevents such a drawback.

4.5.1 Mapping Flutter Eigensolution to Nonlinear Equations

The aeroelastic problem, eq. 4.15, can be seen as a linear homogeneous system in $\{q\}$ and nonlinear in s [52, 53]. So, a normalization rule for the generalized coordinates vector $\{q\}$ can be added to close the problem,

$$\begin{cases} [A(s,V_\infty)]\,\{q\} = 0 \\ \dfrac{1}{2}\,\{q\}^T\,[W]\,\{q\} = 1 \quad . \end{cases} \tag{4.16}$$

The obtained nonlinear system can be solved through the *Newton-Raphson* method. Linearizing around a reference solution $\{q_0\}$ and s_0 we obtain,

$$\begin{bmatrix} [A(s_0,V_\infty)] & \dfrac{\partial[A(s,V_\infty)]}{\partial s}|_{s_0}\,\{q_0\} \\ \{q_0\}^T\,[W] & 0 \end{bmatrix} \begin{Bmatrix} \{\Delta q\} \\ \Delta s \end{Bmatrix} = \begin{Bmatrix} -[A(s_0,V_\infty)]\,\{q_0\} \\ 1-\dfrac{1}{2}\,\{q_0\}^T\,[W]\,\{q_0\} \end{Bmatrix} . \tag{4.17}$$

Such an approach allows to compute the eigenvalue and the eigenvector all at once. Starting from $V_\infty = 0$ with $\{q\} = \{q_0\}$ and $s = s_0$, *i.e* the structural solution, $V_\infty - \omega$ and $V_\infty - g$ diagrams can be drawed. The procedure must be repeated starting from each structural eigenvalue avoiding any problem with intersecting curves. Since the aerodynamic transfer functions matrix $[H_{am}(k)]$ is known for a set of reduced frequencies only a proper interpolation technique must also be implemented. A linear interpolation will be used.

Chapter 5

Wake Generation on Unstructured Grids

5.1 Motivation

To describe lifting bodies a potential flow formulation imposes to model a wake line|surface in the domain. Such a boundary must be contained in the grid which discretizes the fluid surrounding the body. Enforce the boundary at the same time of the grid generation can be trivial in some cases, as airfoils or isolated wings, and hard in other cases, as wing-fuselage combinations, multiple wings vehicles and whole aircrafts. The best strategy to treat the latters could be to apply the cuts required to model single or multiple wakes after a generic unstructured grid generation.

Mesh cutting refers to the process of extracting subparts or components from an existing mesh. It is also known variously as mesh segmentation, mesh partitioning, and mesh scissoring. The cutting operation is of great practical importance in mesh editing. It has been proven useful in many mesh related processing and applications.

With the fast evolution in Computer Graphics and Digital Geometry Processing, mesh cutting serves no longer only to simple tasks such as splitting a mesh into two components or trimming a mesh, but also plays a very important and essential role in higher-level mesh processing operations such as segmentation. Mesh segmentation, like image segmentation, is the process of partitioning a mesh into more visually simple and meaningful components. It has recently become of interest and a key ingredient in many mesh manipulation algorithms [60, 61]. Quite often, these mesh processing operations can improve the result of some advanced techniques such as automatic texture atlas generation, geometry images and making papercraft toys from meshes. Therefore, a good mesh cutting technique is very important.

The garment industry is also involved by the problem. Modern garment CAD methods include 3D human body measurement and modeling, 3D garment design on digital human models, 3D draping simulation, and 2D pattern generation from 3D space. The last operation requires the cut of a 3D surface built on the human body [62].

In modern interactive simulation and modeling environments the ability to cut three-dimensional geometry in real time is also of fundamental importance. This creates the need for efficient cutting algorithms that process the underlying representation. Such methods can be utilized in a wide spectrum of applications including surgical interventions, free form modeling or scientific visualization. In surgery simulation, for instance, interactive cutting algorithms enable the dynamic simulation of scalpel intersections that open immediately behind the scalpel [63]. In the case of free-form modeling or sculpting, dynamic cutting supports a precise positioning and guidance of a cutting tool. In scientific visualization, real-time cutting algorithms create new opportunities for the interactive analysis of volume data sets.

The cut of a three-dimensional solid, however, changes the topology of the underlying data structure and thus poses a great technical challenge. The complexity of a cut algorithm largely depends on the underlying discretization. Our focus is on treat unstructured tetrahedral meshes. The dynamic modeling of intersections and topological changes in such meshes is non-trivial. The methodologies proposed in computer graphics refer to 3D triangular surfaces only. On the other side, real-time techniques involved in surgery simulations are oversized with respect to our purposes. Moreover, aerodynamic grids require *ad hoc* handling of internal boundaries in order to connect the desired wake to the body. So, a special tool to generate a bounded surface, *i.e.* the wake, on an unstructured mesh has been realized.

5.2 Generic Grids

The cut of an unstructured tetrahedral grid according to a generic unbounded surface is treated. The two-dimensional (2D) case can be simply inferred from the three-dimensional (3D) one. The topologically simplest entity which can build a surface is the triangle defined in a 3D domain. On the other side, the topologically simplest entity which builds a tetrahedral grid is the segment, *i.e.* the single tetrahedron edge. So, the cut operation concerns the more simple intersection between triangles and segments.

The procedure iterates over the triangles which form the surface. The *i-th* triangle belongs to the *i-th* plane s^i identified by a normal and a constant,

$$s^i : n_x^i x + n_y^i y + n_z^i z + q^i = 0. \tag{5.1}$$

The distance of the *j-th* point p_j from the *i-th* plane can be easily computed,

$$d_j^i = n_x^i x_j + n_y^i y_j + n_z^i z_j + q^i = 0. \tag{5.2}$$

For every segment of the grid the distances $d1$ and $d2$ of the segment vertices from the plane which contains the generic triangle are computed, as shown in Figure 5.1.

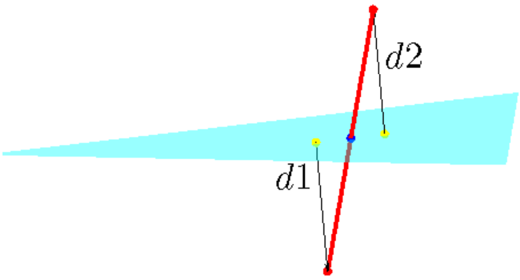

Figure 5.1: Cut interpretation

If $d1 \cdot d2 < 0$ and the intersection point belongs to the triangle the segment intersect the triangle. No special local search is adopted to find intersections. The single intersection can be handled in two ways: move one segment vertex on the plane or split the segment on the intersection. The better choice is the one which produces the least deterioration of the grid. So, the position of the intersection point within the segment must be evaluated. A normalized coordinate can be defined,

$$u = \frac{|d1|}{|d1 - d2|}. \tag{5.3}$$

If $|u - 0.5| > \varepsilon$ the closest vertex must be moved on the intersection (Figure 5.2), where ε is a prescribed tolerance.

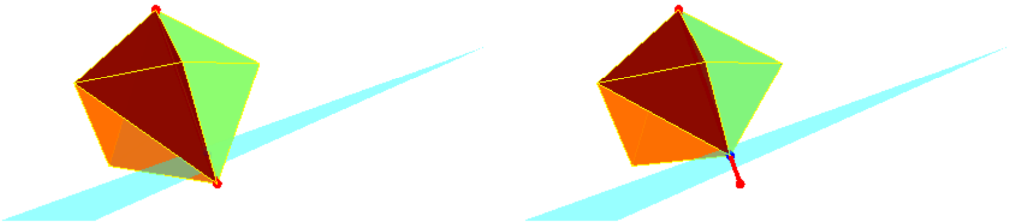

Figure 5.2: Moving operation

The displacement required to move a node to a triangle can be performed by keeping fixed all other nodes or in an elastic way (locally at least). The first way was chosen to preserve computational efficiency. Unfortunately, moving an isolated node could lead to the inversion of some surrounding element, *i.e.* the volume of some tetrahedron can become negative. So, when a node must be moved the volume of the surrounding tetrahedrons in the new configuration must be evaluated. If any volume becomes negative the position of the node must be locked. Figure 5.3 shows, for a test case, the amount of locked nodes in relation with the prescribed cut value ε. The locking criterion more and more reduces the efficiency of the trimming operation as the cut parameter ε decreases. A value of 0.25 for ε could represent a good compromise.

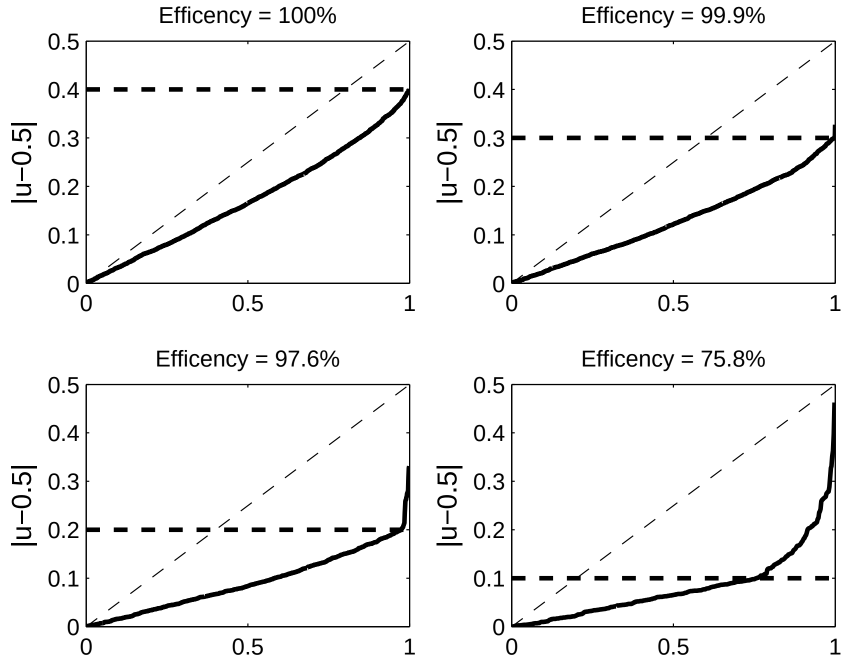

Figure 5.3: Locking of nodes

Now, all the remainder intersected segments must be splitted over the intersection (Figure 5.4).

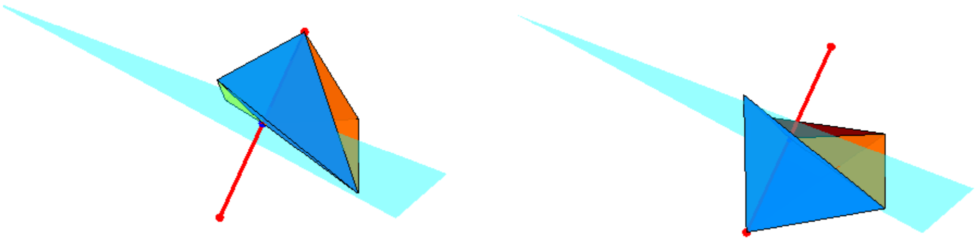

Figure 5.4: Splitting operation

Each splitting operation generates a new node, which automatically belongs to the prescribed surface, and new tetrahedrons. The moving operation and the splitting operation must be performed for each triangle which forms the cutting surface.

A generic application of the above described cutting technique is here presented. Figure 5.5 shows a spherical grid which consists of 230k tetrahedrons cut by three different surfaces.

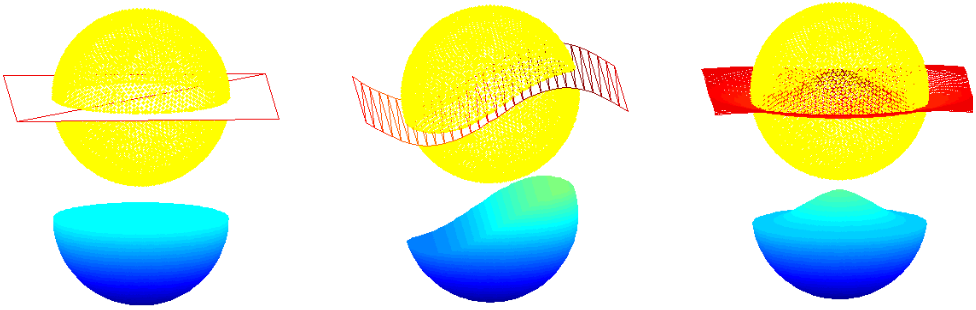

Figure 5.5: Cut examples for a spherical grid

Table 5.1 collects the data for these analyses. Referring to Figure 5.5, an ID is associated to each cutting example starting from the left hand side.

ID	triangles	CPUtime
1	2	40 sec.
2	60	70 sec.
3	7200	15 min.

Table 5.1: Data of cutting examples.

The proposed procedure reveals a poor computational efficiency when the spatial discretization of the cutting surface is comparable to the grid discretization, as the example related to ID 3 in table 5.1. In such conditions the simple searching algorithm used results unsuitable. More efficient tree search algorithms could improve its performances. However, our applications are characterized by a reduced number of triangles, as the examples related to ID 1 and 2 in table 5.1, so the adopted searching algorithms may be reputed appropriate.

5.3 Aerodynamic Grids

Applications to aerodynamic grids require some additional processing in order to handle a bounded cutting surface, *i.e.* the wake.

Referring to Figure 5.6, the trailing edge (red) and internal wake boundaries (blue) must be identified and additional triangles (green) must be introduced to ensure internal wake boundaries.

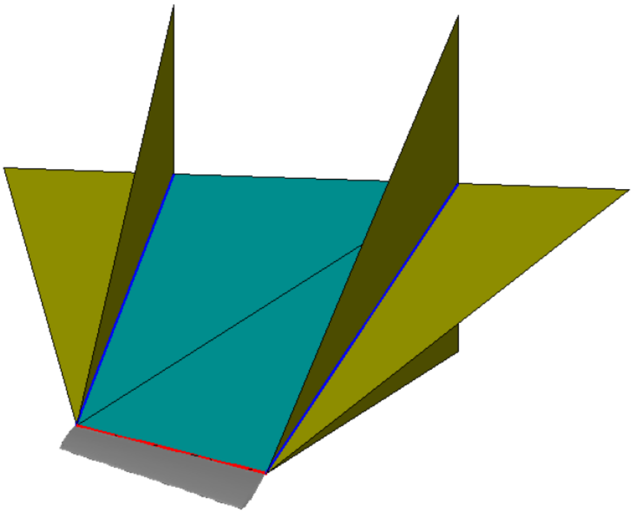

Figure 5.6: Wake generation for Agard 445.6 wing

The above mentioned cut technique was applied to a tetrahedral grid modelling an AGARD 445.6 wing. Figure 5.7 shows the obtained wake. The cutting operation seems to preserve the isotropy of the starter grid leading to a good wake discretization. Further more complex wake cuts for the HIRENASD wing and the A320 aircraft will be presented in the next chapter.

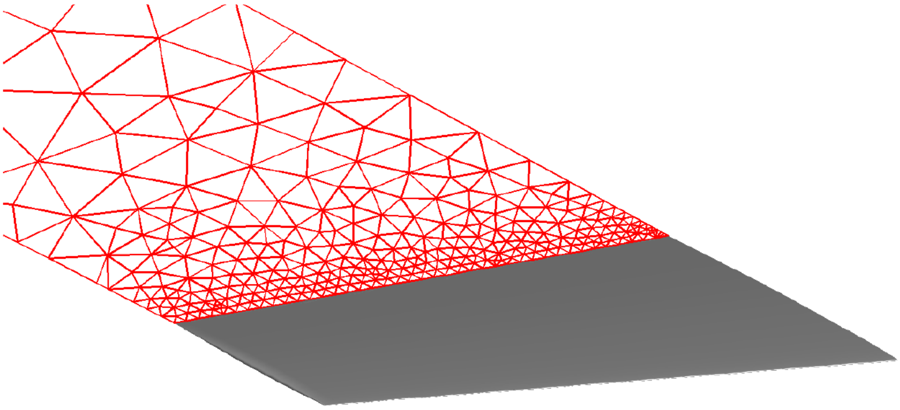

Figure 5.7: Agard 445.6 wake

Chapter 6

Numerical Results

To validate the here proposed formulation and its implementation, some results obtained with the developed code, named S^T (TRANSonic POtential baSED Solver), are presented in the following. The analyses have been performed on a 2.33 Ghz CPU and 800 Mhz RAM. Transonic analyses have been carried out using two N-R steps and a matrix-free GMRES linear solver, restarted every 20 inner iterations, with a tolerance of 10^{-3} for 3 times at most. The single preconditioner adopted for the two-dimensional (2D) analyses was related to an undisturbed flow at the asymptotic Mach number. The line|surface which represents the wake is part of the domain discretization and is not trimmed according the motion field. For complex three-dimensional (3D) geometries and available generic unstructured grids the wake has been realized by means of the previously described procedure. The influence of the wake location within the domain has not been investigated. The fluid-structure interface for aeroelastic analyses has been realized with an available MLS routine [58]. Unsteady solutions aimed at flutter prediction were performed with fixed meshes by imposing the proper transpiration on the solid boundary. In other unsteady analyses the grid has been deformed in an elastic analogy manner with the grid represented as a linear elastic continuum. The proposed ALE formulation frees from any limitation from the mesh motion and structural motion matching to grant Geometric Conservation Law (GCL) [37]. The implementation of the quadratic formulation is limited to 2D domains.

6.1 2D Analyses

The first analysis concerns the verification of the accuracy for the linear and quadratic formulation. Figure 6.1 stresses the difference between the two formulations. A coarse grid, consisting of about 6k triangles and 80 nodes on the solid boundary, models the domain around a NACA 0012 airfoil. A fine grid is obtained by dividing each triangle of the coarse grid in four triangles and by adding midpoint nodes. Figure 6.1 shows not so unexpected results. With the same number of variables, guaranteed by the way in which the fine grid was generated, the two formulations lead to perfectly matched results. Instead, on the coarse grid, the linear formulation misses the strong pressure gradient at the leading edge for the subcritical condition and the sharp shock in the transonic case.

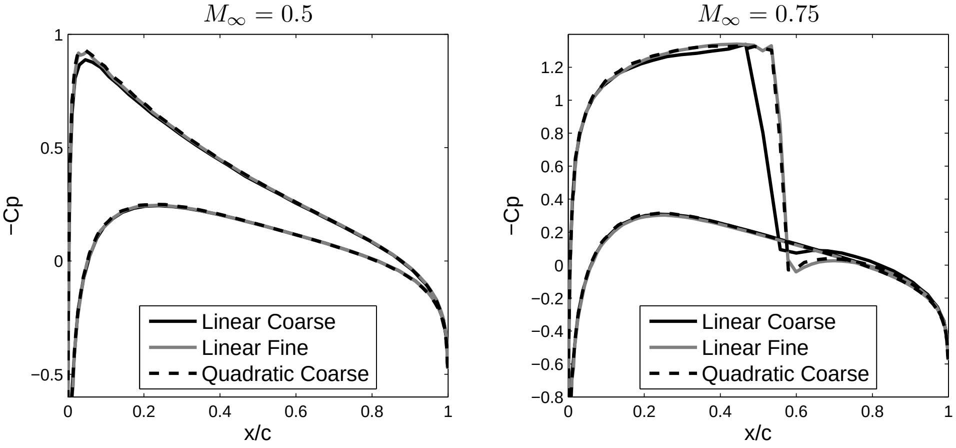

Figure 6.1: Pressure distribution over NACA 0012 airfoil for Linear and Quadratic formulations, $\alpha = 2\,\mathrm{deg}$

Nevertheless, the computational cost of the quadratic formulation is slightly greater than a linear formulation with the same number of variables. Moreover, the quadratic formulation could lead to a wrong position for sharp shocks due to the low number of nodes on the solid boundary. A local mesh refinement or deformation could improve the shock capturing but such techniques are not used in the present work.

The proposed ALE formulation is here compared to the most usual one using relative fluxes. Figure 6.2 shows the results for an oscillating NACA 0012 airfoil in subcritical conditions. The grid has been deformed as a continuum with imposed boundary motions with different values of the Poisson coefficient in order to obtain deformation fields with different divergence of the control volumes. The usual ALE formulation (ALE 1) has been applied with no care on the choice of the proper integration scheme needful to grant the volumes conservation. Such a carelessness becomes more relevant as the local domain divergence increases, *i.e.* when the Poisson coefficient decreases. Instead, using the same integration scheme, the proposed ALE formulation (ALE 2) results independent from the deformation parameters avoiding the need to preserve the divergence of the control volumes. Such considerations well reveal the advantages of the proposed ALE formulation.

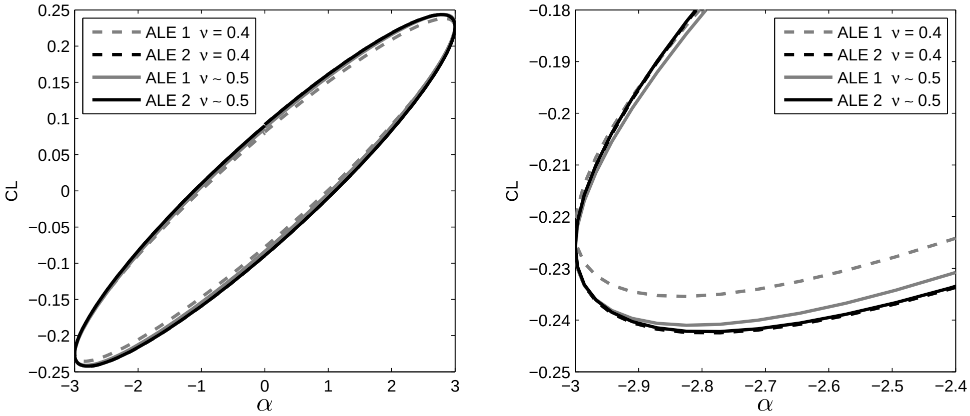

Figure 6.2: Lift coefficient of NACA 0012 airfoil, $M_\infty = 0.5$, $\omega = 1$

Table 6.1 should well confirm the improvements provided by the presented entropy correction for a NACA 0012 airfoil modeled with three spatial discretization, applied to one (1) or two (2) layers of elements adjacent to the body-wake surface. The corrected lift coefficients are compared with the corresponding isentropic (0) values and the results obtained with the AeroFoam [64] (AF) Euler solver. The results should thus prove the effectiveness of a linear, in the thickness, approximation of the entropy correction based just on the values at the body-wake and going to zero at the other layer surface. It can be seen also that it can be approximated even with a single layer, being independent from the layer thickness eventually. Therefore the just verified scheme will be applied to all of the subsequent 2-3D analyses to be presented here.

ID	**Nodes**	**Triangles**	**min(h)**	$C_L(0)$	$C_L(1)$	$C_L(2)$	$C_L(\mathrm{AF})$
1	3100	6100	0.0030	0.527	0.415	0.416	0.422
2	11300	22300	0.0015	0.574	0.402	0.403	0.419
3	44900	89200	0.0007	0.575	0.394	0.395	0.416

Table 6.1: Lift coefficient of NACA 0012 airfoil, $M_\infty = 0.75$, $\alpha = 2\,\mathrm{deg}$

The sample Figure 6.3 shows how the entropy correction improves both the strength and position of a strong enough shock over a NACA 0012 airfoil, for the mesh identified as ID 3 in table 6.1.

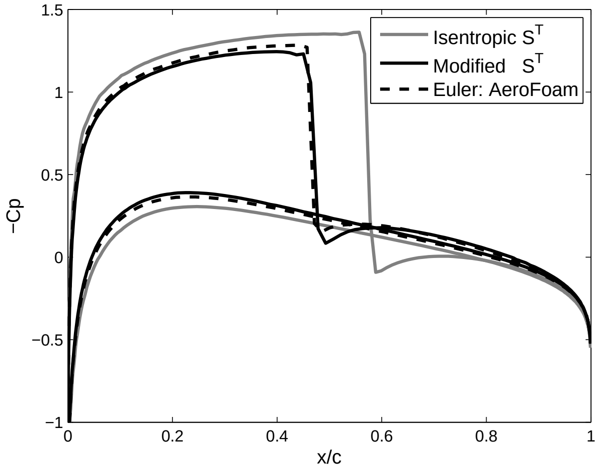

Figure 6.3: Pressure distribution over NACA 0012 airfoil, $M_\infty = 0.75$, $\alpha = 2\,\text{deg}$, CFL = 1000

Figure 6.4 is related to the mesh ID 2 in table 6.1 and demonstrates how the entropy correction tames the strong non-linearities causing possible non-uniquenesses [25, 26] of the lift at high transonic conditions, up to producing a perfect to good match with Euler solutions. It should be remarked that the results related to non corrected applications are either erratic, with an unbearably slow convergence, or diverging.

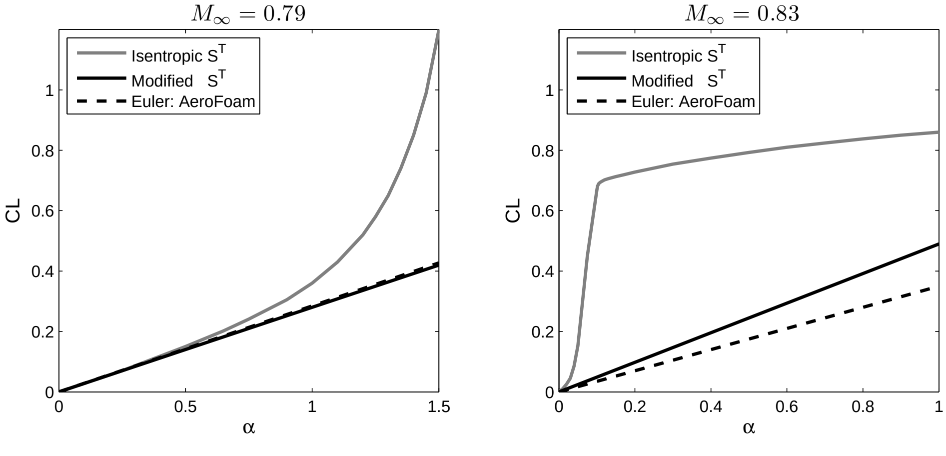

Figure 6.4: Lift versus angle of attack for NACA 0012 airfoil, CFL = 100

A similar comment can be applied to the further added effectiveness in estimating unsteady shock motions using Guderley formula for the ID 1 mesh in table 6.1, as shown in Figure 6.5. Four pitching motion cycles where

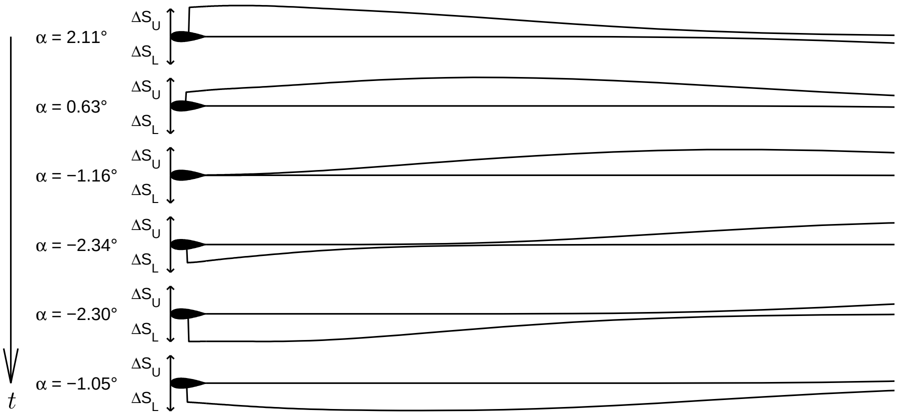

Figure 6.6: Entropy level of oscillating NACA 0012 airfoil, $M_\infty = 0.755$, $\alpha = (.02 + 2.51 \sin(0.1t))\,\mathrm{deg}$

simulated, for a total of 512 steps. The last cycle normal force and pitching moment coefficients are presented in Figure 6.5. The comparison with AeroFoam [64] Euler results should well demonstrate the effectiveness of the correction for unsteady flow conditions. Figure 6.6 illustrates the alternating entropy production on the upper and lower body surfaces as well as its convection along the body-wake surface during the pitching motion.

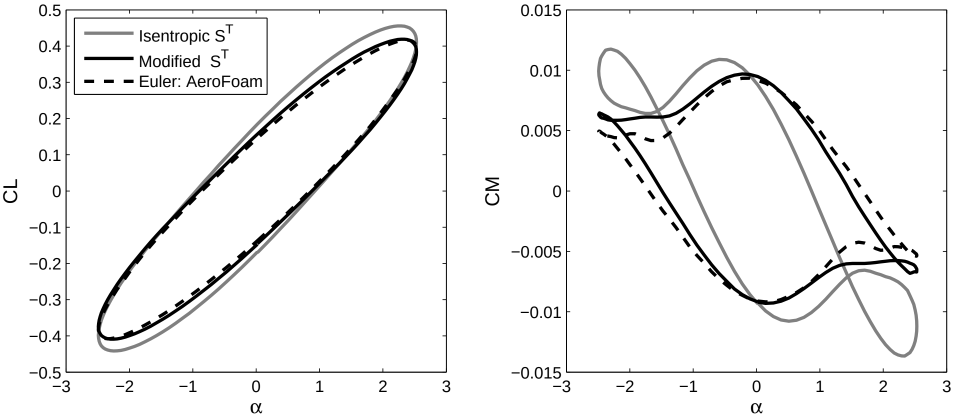

Figure 6.5: Load coefficients of oscillating NACA 0012 airfoil, $M_\infty = 0.755$, $\alpha = (.02 + 2.51 \sin(0.1t))\,\mathrm{deg}$, CFL = 4264

In Figure 6.7 the Mach distribution along the chord of a 2D thin plate is compared with the Prandtl-Mayer expansion theory on the upper surface and the oblique shock theory on the lower surface. A good agreement with analytical results seems to have been achieved, the smearing at the trailing

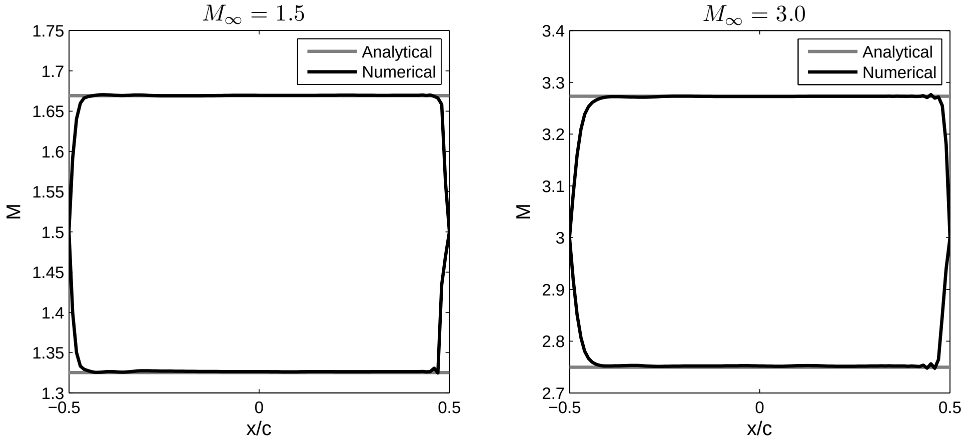

Figure 6.7: Mach distribution over thin plate, $\alpha = 5\,\text{deg}$, CFL $= 100$

and leading edge regions is believed to be consistent with the used spatial discretization (12k nodes, 24k triangles and 100 chord divisions). The steady state condition is reached with the generalization of the modified Newton-Raphson method in 3 time steps with only one internal iteration in about 0.12 seconds.

A thin plate subject to step angle of attack is considered. Figure 6.8 compares the numerical results with those of the linear theory related to a thin plate [65], highlighting the initial transient phase against piston theory [65].

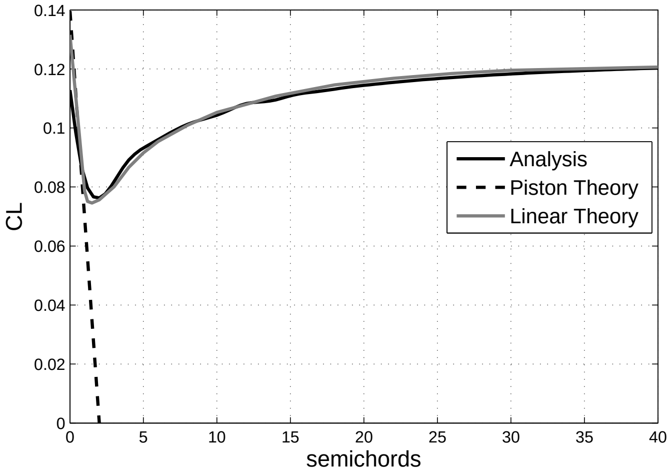

Figure 6.8: Response of thin plate to step angle of attack, $M_\infty = 0.5$, $\alpha = 1\,\text{deg}$

With the same thin plate, the proposed approach can be compared with incompressible Theodorsen's theory [50] for a plunging-pitching 2D plane plate. Theodorsen's harmonic solution provides a benchmark for any newly developed computational fluid dynamics scheme. The plunge motion h and the pitch motion θ are related to the lift coefficient C_L and the moment coefficient C_M (referred to the quarter chord location) in the frequency domain with the reduced frequency k through the aerodynamic transfer functions matrix H_{am}:

$$\left\{ \begin{array}{c} C_L(k) \\ C_M(k) \end{array} \right\} = [H_{\mathrm{am}}(k)] \left\{ \begin{array}{c} h(k) \\ \theta(k) \end{array} \right\} . \tag{6.1}$$

The incompressible condition is approximated with $M_\infty = 0.01$. Figure 6.9 shows a good agreement with Theodorsen's theory.

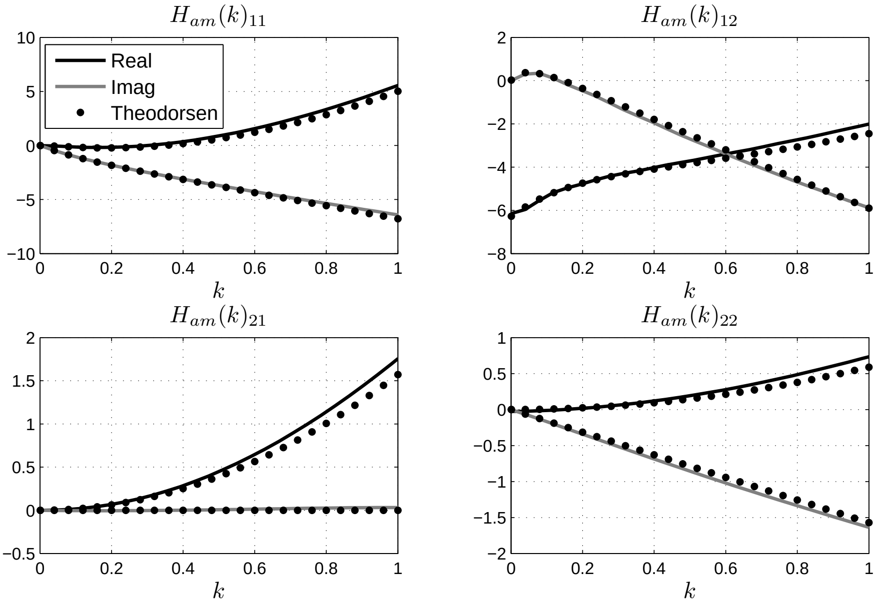

Figure 6.9: Aerodynamic transfer functions matrix of a thin plate, $M_\infty = 0.01$

The above results indicate that the two-field approximation does not lose accuracy at very low Mach numbers. Moreover, the efficient linearization provided by transpiration boundary conditions, coupled to a procedure that allows the determination of aerodynamic transfer matrices through appropriately imposed transient motion [66], allows the use of the proposed approach in transonic flutter analyses based on the strip theory, still used profitably for high aspect ratio wings, in conceptual-preliminary designs especially.

The stability of a plunging-pitching aerofoil is now investigated. Figure 6.10 depicts the treated model. The aerofoil is subject to the aerodynamic loads, the linear and torsion elastic reactions and the inertial reactions.

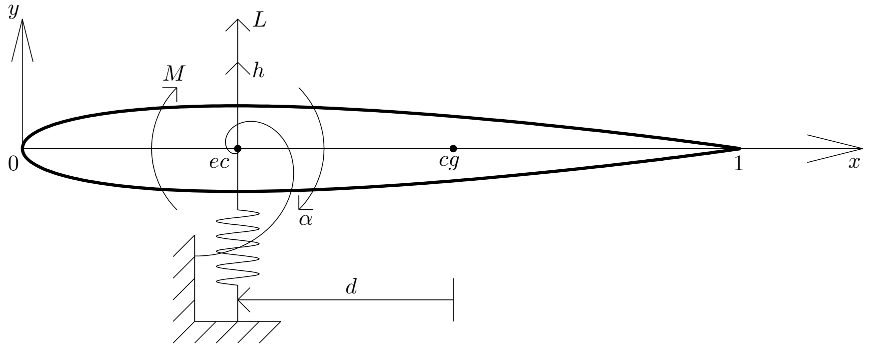

Figure 6.10: Two degrees-of-freedom aerofoil

The dynamics equations of such a model can be arranged as:

$$\begin{bmatrix} m & -S \\ -S & I \end{bmatrix} \begin{Bmatrix} \ddot{h} \\ \ddot{\alpha} \end{Bmatrix} + \begin{bmatrix} k_h & 0 \\ 0 & k_\alpha \end{bmatrix} \begin{Bmatrix} h \\ \alpha \end{Bmatrix} = \begin{Bmatrix} L \\ M \end{Bmatrix}. \tag{6.2}$$

Using the definitions of the first moment of area S, the second moment of area I and the aerodynamic load coefficients C_L and C_M one obtains:

$$\begin{bmatrix} 1 & -d \\ -d & r^2 \end{bmatrix} \begin{Bmatrix} \ddot{h} \\ \ddot{\alpha} \end{Bmatrix} + \omega_\alpha^2 \begin{bmatrix} \omega_r^2 & 0 \\ 0 & r^2 \end{bmatrix} \begin{Bmatrix} h \\ \alpha \end{Bmatrix} = \frac{\rho_\infty V_\infty^2}{2m} \begin{Bmatrix} C_L \\ C_M \end{Bmatrix}. \tag{6.3}$$

After a Laplace transform the system becomes:

$$\left(\begin{bmatrix} 1 & -d \\ -d & r^2 \end{bmatrix} s^2 + \omega_\alpha^2 \begin{bmatrix} \omega_r^2 & 0 \\ 0 & r^2 \end{bmatrix} - \frac{2V_\infty^2}{\pi\mu} H_{am}\left(M_\infty, k\right) \right) \begin{Bmatrix} h \\ \alpha \end{Bmatrix} = 0, \tag{6.4}$$

where the aerodynamic transfer function matrix $H_{am}(M_\infty, k)$ and the mass ratio μ appear. Table 6.2 collects the data for the proposed analysis.

Aerofoil	$\boldsymbol{\mu}$	$\boldsymbol{x_{cg}}$	$\boldsymbol{d}$	$\boldsymbol{r}$	$\boldsymbol{\omega_r}$
NACA 0012	100	0.5	0.1	0.2695	0.343

Table 6.2: Data for a two-dof aerofoil.

In Figure 6.11 the results obtained with the isentropic (S^T) and the non isentropic version ($S^T k$) of the code are compared to those obtained with another full potential code (FP) and its boundary-layer-iteration counterpart (FPv) [35].

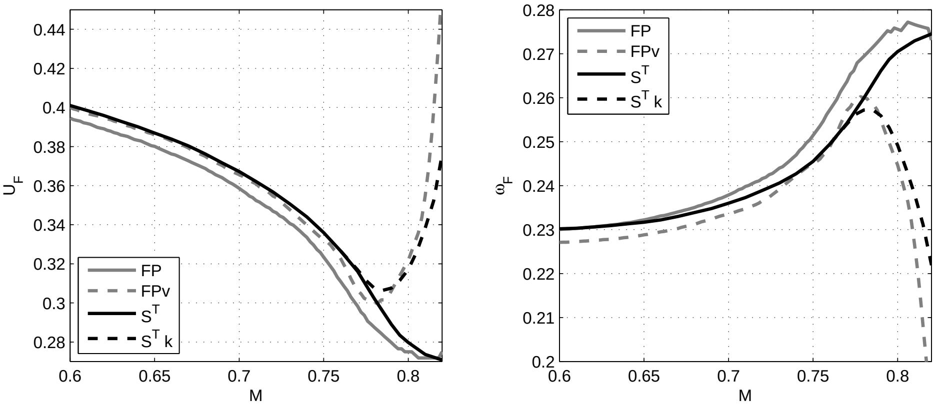

Figure 6.11: Flutter for a two-dof NACA 0012 airfoil, $U = \frac{2V_\infty}{\omega_\alpha\sqrt{\mu}}$, $\omega = \frac{\Im s}{\omega_\alpha V_\infty}$

Both the entropy correction and the boundary layer iteration ensure the usual transonic dip. These results prove again the effectiveness of the proposed entropy correction.

Finally, table 6.3 shows the computational efficiency of the 2D code. Each analysis ends when a steady state lift is reached within a relative error of 10^{-4}. An outstanding efficiency of the code for subcritical conditions could be remarked.

Regime	M_∞	α	**Nodes**	**Method**	**CPUt [sec]**
subcritical	0.63	2	2252	$L_0U_0X = R$	0.02
transonic	0.75	2	2252	GMRES	0.87
subcritical	0.60	1	8881	$L_0U_0X = R$	0.09
transonic	0.75	2	8881	GMRES	9.55

Table 6.3: CPUtime for 2D steady analyses on NACA 0012 airfoil

6.2 3D Analyses

The first 3D transonic verification is related to the well known ONERA M6 wing at a Mach number of 0.8395 and an angle of attack of 3.06 deg. The discretization adopted consists of 139k nodes and 700k tetrahedrons. With a CFL of 10000 the steady state condition is reached in 20 time steps and about 200 seconds. Figure 6.12 shows the familiar "Lambda shock" formed on the upper surface of the wing.

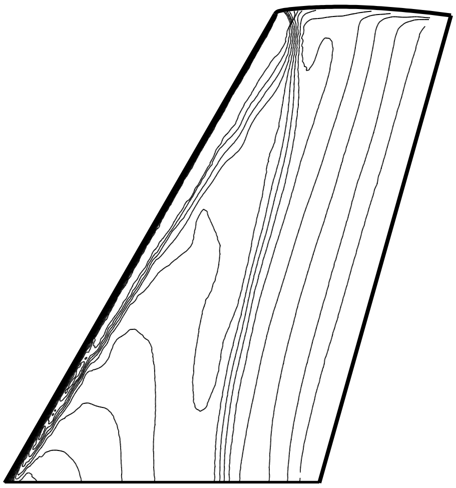

Figure 6.12: Pressure contours on the upper surface of M6 wing using S^T, $M_\infty = 0.8395$, $\alpha = 3.06\,\text{deg}$, CFL = 10000

Figure 6.13 presents the comparison of a few pressure distributions provided by S^T against their wind tunnel (WT) counterparts [67] and the results of AeroFoam (AF) Euler solver [64].

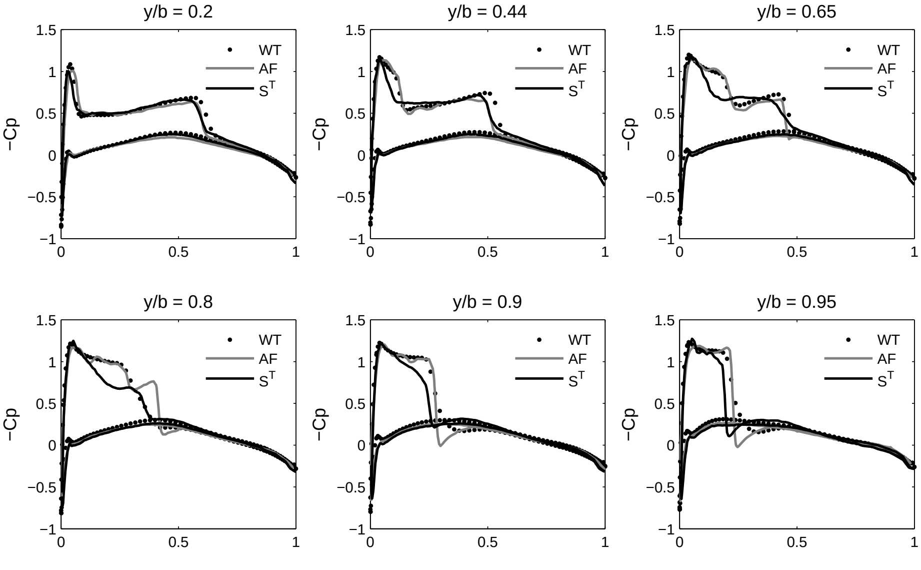

Figure 6.13: Pressure distribution over M6 wing, $M_\infty = 0.8395$, $\alpha = 3.06\,\text{deg}$, CFL = 10000

It is worth noting that because of the relatively weak downstream shock (local $M_{max} < 1.2$) the entropy correction had no appreciable effect.

A non-twisted wing with a NACA 0012 airfoil, aspect ratio 9.4, taper ratio 0.7 and a sweep of 10 deg at the $c/4$ line is then used for a set of 3D numerical test covering sub-supersonic asymptotic flow conditions. The flow field is discretized with 156k nodes and 784k tetrahedrons. The extension to steady supersonic analyses has the aim of showing both how even unreasonably high CFL numbers, as high as 10000 again, do not hinder the stability of the solution method and the robustness of the preconditioner scheme adopted. Subsonic results are not reported for sake of brevity, as they will provide much the same outcome of the already shown 2D sample case with the same profile. Of much significance instead are the results for a significantly detached shock associated to the inappropriate use, purposely made, of the relatively blunt nose NACA 0012 profile. That should be well demonstrated by the sample pressure distributions for $M_\infty = 1.2$, depicted in Figure 6.14, comparing potential results, obtained by using a preconditioner based on an undisturbed flow at $M_\infty = 0.8$, against AeroFoam (AF) Euler solver [64]. What shown should indirectly confirm also the validity of the new extended sub-supersonic stability analysis, carried out in a one-dimensional linearized form only, even for a highly nonlinear 3D supersonic case.

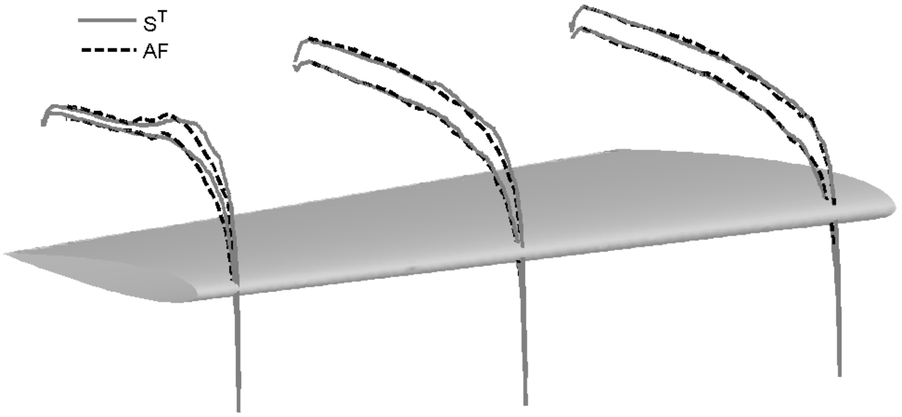

Figure 6.14: Pressure distribution over NACA wing, $M_\infty = 1.2$, $\alpha = 2\,\text{deg}$, CFL = 10000

The CPU time of various steady analyses conducted for the above mentioned wing at different asymptotic Mach numbers and constant angle of attack of 2 deg is depicted in Figure 6.15. The preconditioner for the all calculations, covering quite a wide Mach range, was computed at $M_\infty = 0.8$, its incomplete LU factorization requiring about four minutes. Each analysis is conducted with two N-R iterations and the number of timesteps required to achieve a steady state lift within a relative error of 10^{-4}.

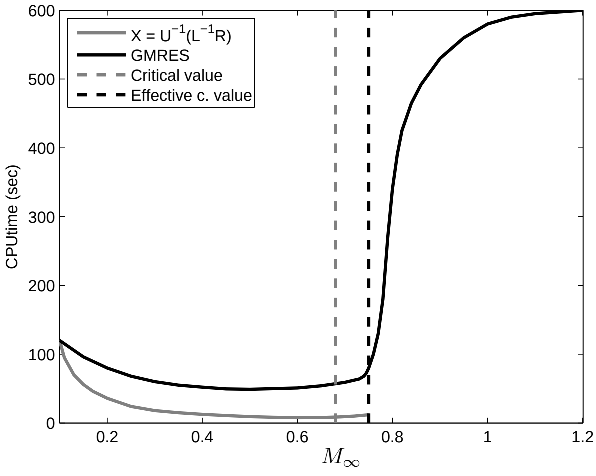

Figure 6.15: CPUtime (sec) for 3D steady analyses of a 156k nodes wing at constant preconditioner

We can clearly see an effective numerically critical asymptotic Mach number, greater than the critical subsonic Mach number, which causes quite a numerical effectiveness loss of the solution procedure related to HFs and the rapid growth of the GMRES effort. It is important to emphasize again that the mentioned Figure well proves that the not so strongly nonlinear behavior of HFs allows the present method to be close to being competitive with panels formulations. Referring to table 6.3 it is possible to extend the above remark to 2D flows also.

The numerical results for the aeroelastic benchmark test problem of computing the flutter boundary for the AGARD 445.6 wing [68] is here presented. The aerodynamic transfer functions matrices resulting from a blended step input computed with AeroFoam (AF) and S^T at different asymptotic Mach numbers are shown in Figures 6.16, 6.17 and 6.18. Considering that those reference data were obtained on a slightly finer aerodynamic grid the agreement is satisfactory. Performing a parametric stability analysis of the linear(ized) time-invariant aeroelastic dynamic system it is possible to build the $V-\omega$ and $V-g$ diagrams shown in Figures 6.19, 6.20 and 6.21. In good agreement with the numerical and experimental data available in literature the first normal mode of vibration is the unstable one and as the flutter point is approached the typical frequency coalescence phenomenon is observed.

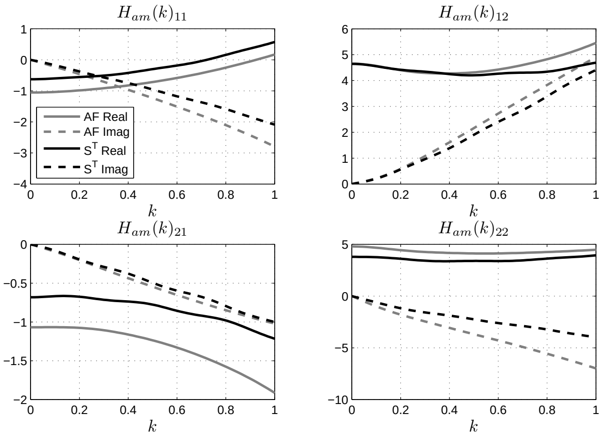

Figure 6.16: H_{am} of AGARD 445.6 wing at $M_\infty = 0.678$

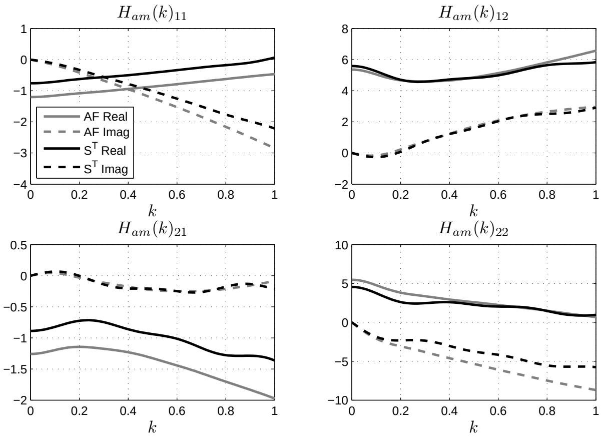

Figure 6.17: H_{am} of AGARD 445.6 wing at $M_\infty = 0.960$

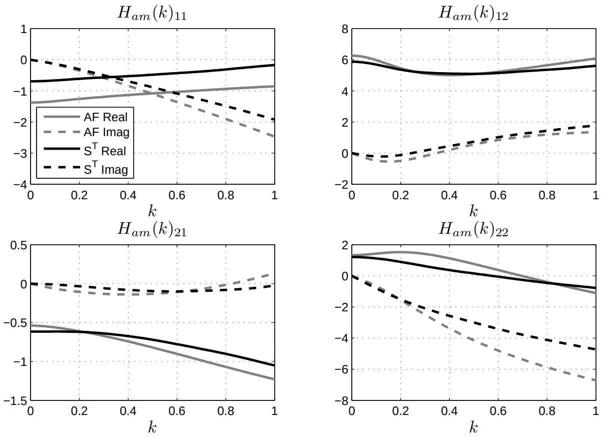

Figure 6.18: H_{am} of AGARD 445.6 wing at $M_\infty = 1.140$

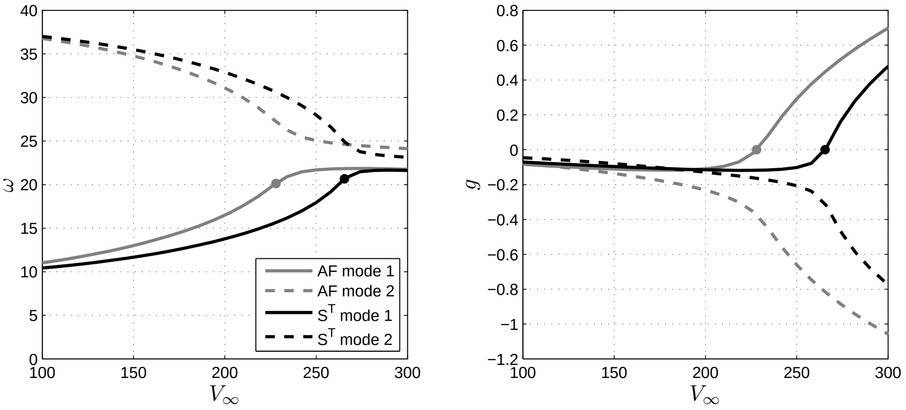

Figure 6.19: $V\omega$ and Vg diagrams of AGARD 445.6 wing at $M_\infty = 0.678$

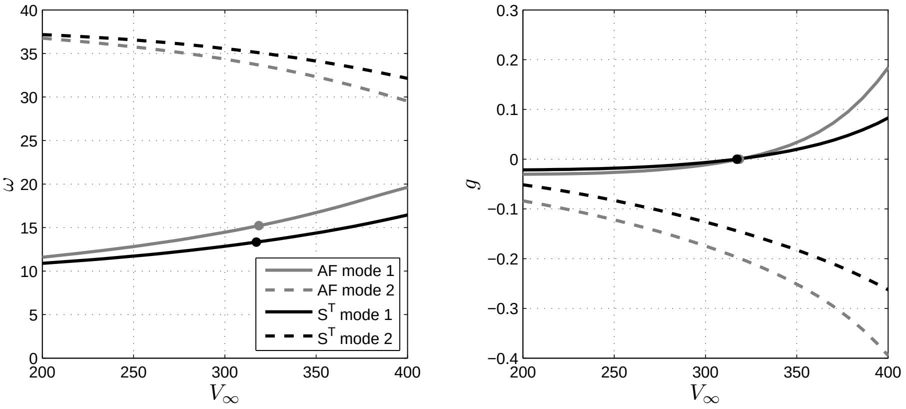

Figure 6.20: $V\omega$ and Vg diagrams of AGARD 445.6 wing at $M_\infty = 0.960$

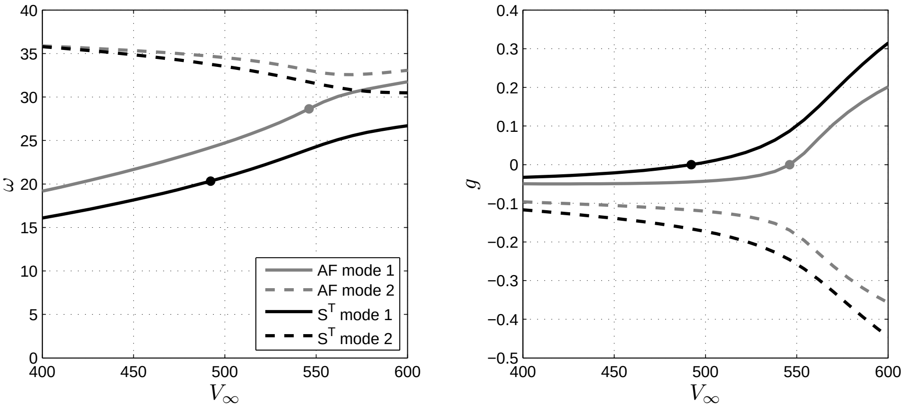

Figure 6.21: $V\omega$ and Vg diagrams of AGARD 445.6 wing at $M_\infty = 1.140$

Finally, in Figure 6.22 the adimensional frequency ratio $I_\omega = \omega_F/\omega_\alpha$ and flutter index $U_F = V_F/(L_a\omega_\alpha\sqrt{\mu})$ are presented, where ω_α is the first torsional natural pulsation and μ is the mass ratio. A good agreement with the experimental data is observed in the transonic dip but the flutter point is generally overpredicted.

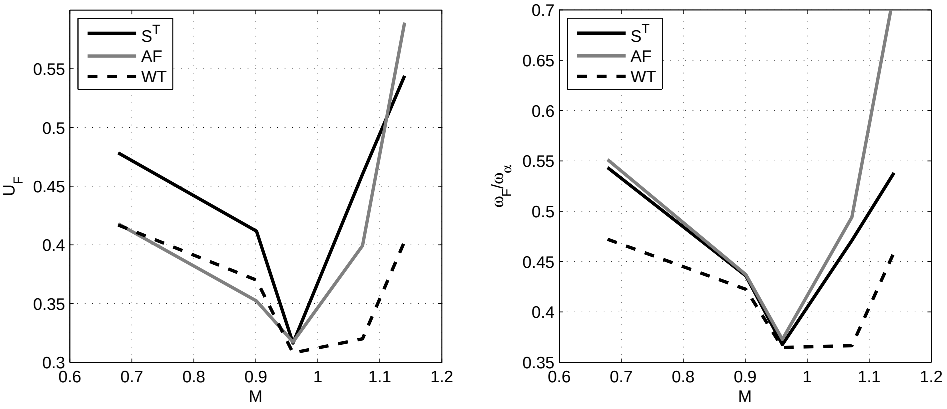

Figure 6.22: Flutter speed and frequency indices for AGARD 445.6 wing

The last two analyses concern a restrained and a free-flying static trim. For the restrained case, the attachment provides the balancing forces and moments according to the aerodynamic and inertial loads working on the model. The static trim of HIRENASD wing [59] was investigated. The flow field is discretized with 138k nodes and 674k tetrahedrons. Figure 6.23 shows the wake resulting from the cutting technique described in the previous chapter.

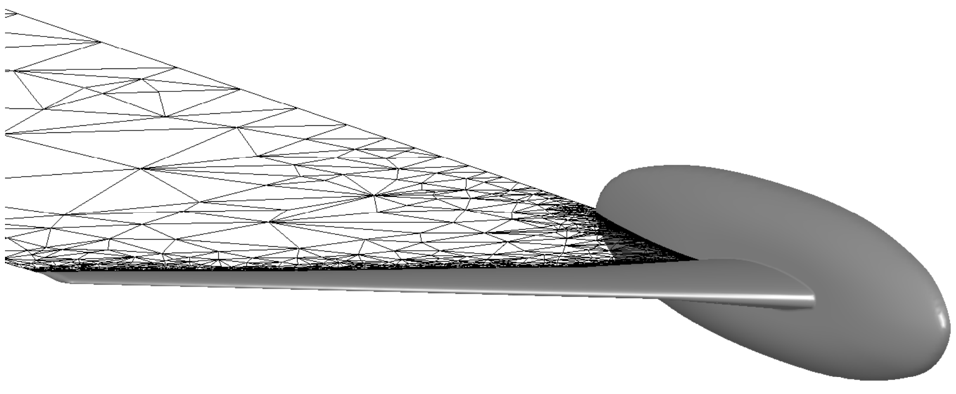

Figure 6.23: HIRENASD wing wake

A normal modes analysis has been conducted with the available beam model of the wing and the moving least squares (MLS) interface was realized. The normal modes has been used to model the static deformation. The aeroelastic analysis has been conducted by iterating the closed-loop connection between the aerodynamic forces and the structural deformation.

The static deformation of the wing at the transonic condition related to the asymptotic Mach number of 0.8 is investigated. Figure 6.24 shows, for the angle of attack of 1.5 deg, the obtained results (S^T) against AeroFoam (AF) results (Euler and RANS) and other numerical RANS results (FUN3D) and wind tunnel data (WT) available in [59].

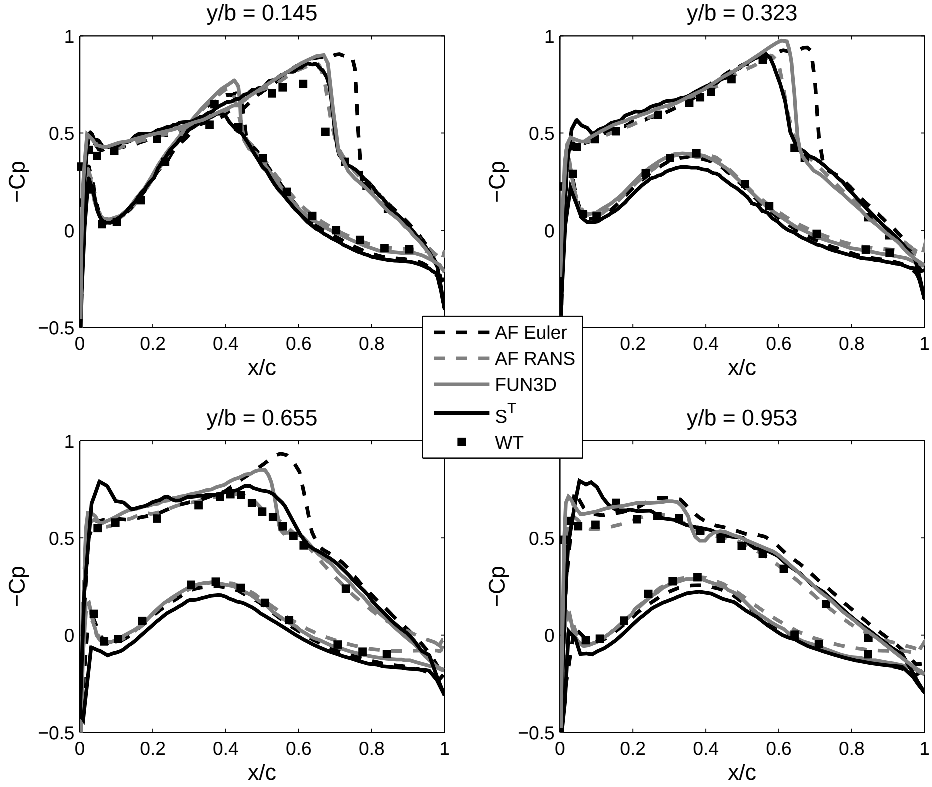

Figure 6.24: Pressure distribution over HIRENASD wing, $M_\infty = 0.8$, $\alpha = 1.5\,\text{deg}$

The Euler solution (AF) leads to a sharper shock and so an higher load on the wing thanks to a finer grid. Figure 6.25 confirm such a consideration by showing the value of the vertical displacement of the wing tip for different angles of attack. The higher dissipation leads our calculation to more realistic results, *i.e.* closer to RANS results, but, obviously, this is not a desirable effect.

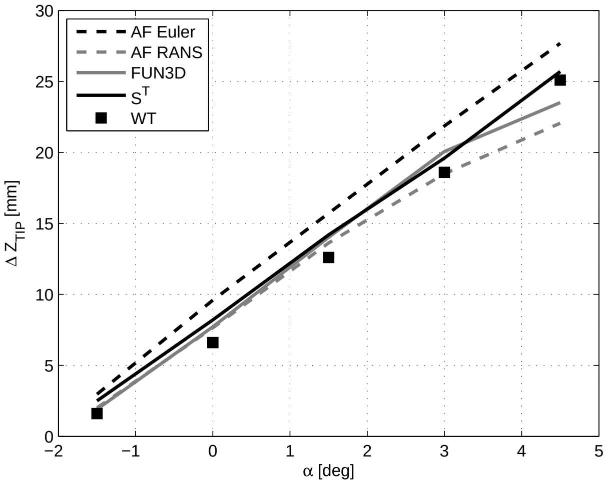

Figure 6.25: Wing tip vertical displacement of HIRENASD wing, $M_\infty = 0.8$

The static trim of A320 aircraft is now considered. For the case of a free-flying object like an aircraft, the inertial and the aerodynamic forces must balance each other. Focusing on the longitudinal trim problem, assuming that the available engine thrust is sufficient for the equilibrium along the x-direction to be satisfied a-priori and neglecting the engine thrust contribution to the pitching moment we have the following set of conditions:

$$\begin{cases} F_z(M_\infty, \alpha, \delta, \{q\}) = nW \\ M_{y,CG}(M_\infty, \alpha, \delta, \{q\}) = 0 \end{cases} \tag{6.5}$$

where the dependence from the angle of attack α, the elevator rotation δ and the structural deformation $\{q\}$ has been expressed. The trim problem, eq. 6.5, could be solved in an iterative way during the aerodynamic time marching analysis by neglecting the effect of the deformation. It is then necessary to solve the non-linear rigid trim problem by means of modified Newton-Raphson method iterations through an approximation of the Jacobian matrix of the rigid trim conditions:

$$\begin{Bmatrix} F \\ M \end{Bmatrix}^k + \begin{bmatrix} F_{/\alpha} & F_{/\delta} \\ M_{/\alpha} & M_{/\delta} \end{bmatrix} \begin{Bmatrix} \Delta\alpha \\ \Delta\delta \end{Bmatrix}^{k+1} = \begin{Bmatrix} nW \\ 0 \end{Bmatrix}. \tag{6.6}$$

In order to prevent excessive overshoots during the time marching solution a relaxation parameter β must be applied,

$$\begin{Bmatrix} \Delta\alpha \\ \Delta\delta \end{Bmatrix}^{k+1} = \beta \begin{bmatrix} F_{/\alpha} & F_{/\delta} \\ M_{/\alpha} & M_{/\delta} \end{bmatrix}^{-1} \left(\begin{Bmatrix} nW \\ 0 \end{Bmatrix} - \begin{Bmatrix} F \\ M \end{Bmatrix}^{k} \right). \tag{6.7}$$

Figure 6.26 shows the structural nodes which constitute the available beam model of the aircraft. Geometric data and details about the structural model are available in [69]. Table 6.4 shows the obtained modal base. The MLS interface was also realized.

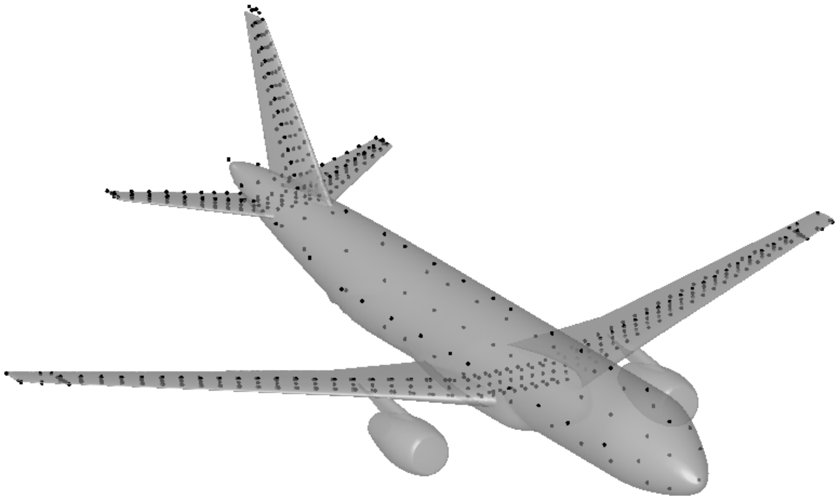

Figure 6.26: Structural nodes of an A320

Mode	**Frequency [Hz]**	**Description**
α	0	rigid pitch
δ	0	rigid elevator rotation
7	2.34	first bending
10	5.31	second bending
11	5.57	in-plane bending
13	6.62	first torsional
15	8.33	first bending-torsion
17	8.74	second bending-torsion

Table 6.4: Modal base used for nonlinear trim analysis of an A320

The flow field is discretized with 80k nodes and 392k tetrahedrons. Figure 6.27 shows the main wake and the tail wake obtained by means of the wake generation routine. The vertical tail wake has not been generated because only longitudinal trim has been investigated. The poor isotropy of the grid is well deducible from the wakes discretization. However, such a discretization, needed to reduce computational costs, has not considerably affected the numerical convergence to the steady state.

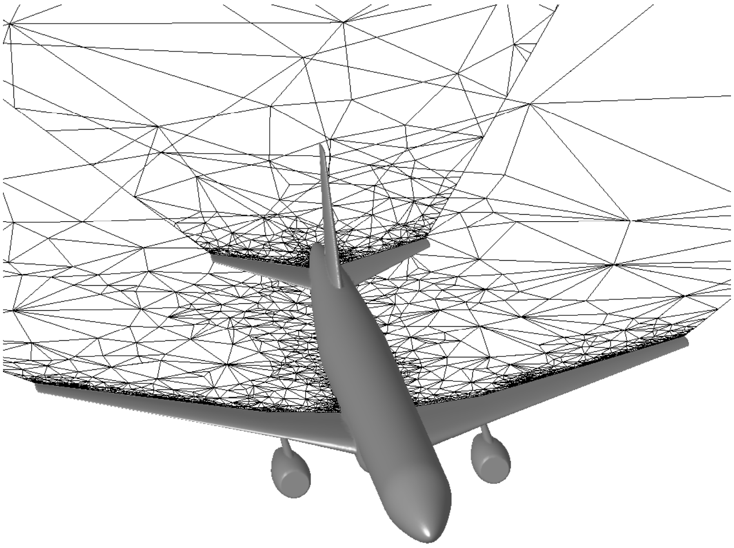

Figure 6.27: Wakes of an A320

The trim condition related to a unitary load factor n and the asymptotic Mach number of 0.78 is investigated. In order to apply the linearized iteration, eq. 6.7, a suitable approximation of the Jacobian matrix must be realized. The Jacobian matrix can be obtained through a finite difference approach by choosing a proper perturbation ε and performing three approximated solution with $(\alpha = \delta = 0)$, $(\alpha = \varepsilon, \delta = 0)$ and $(\alpha = 0, \delta = \varepsilon)$. Figure 6.28 shows the convergence history of the aerodynamic loads during the coupled time marching solution. The chosen relaxation parameter of 0.25 grants a smooth convergence in only 22 iterations by totalizing a CPUtime of about 7 minutes. Table 6.5 compares the obtained results (S^T) with those of the Euler solver (AF) in terms of the angle of attack α the elevator rotation δ and the first bending modal coordinate q at the trimmed condition. The most relevant difference concerns the rotation of the elevator control surface. Such a difference can be imputed to the different grid or the different mesh deforming technique adopted in the two analyses. Finally, Figure 6.29 shows the trimmed deformed condition. The aircraft attitude and deformation and the boundary grid are well appreciable.

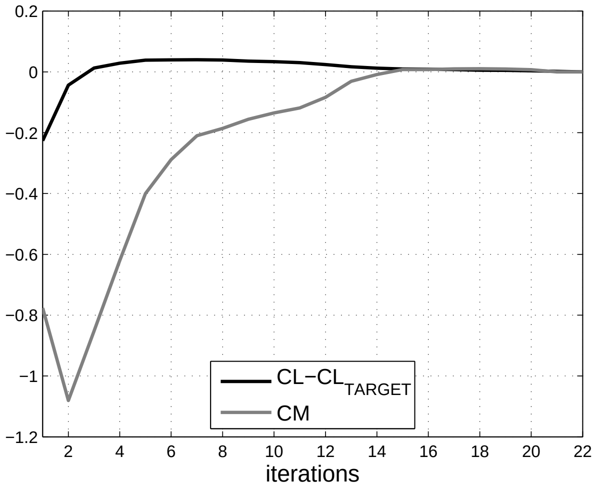

Figure 6.28: Convergence of trim analysis of an A320, $M_\infty = 0.78$, $n = 1$, $\beta = 0.25$

	$\boldsymbol{\alpha}$**[deg]**	$\boldsymbol{\delta}$**[deg]**	$\boldsymbol{q}$**[-]**
$\boldsymbol{S^T}$	3.12	-8.78	31.8
AF	3.80	-5.37	28.2

Table 6.5: Trim parameters of an A320, $M_\infty = 0.78$, $n = 1$

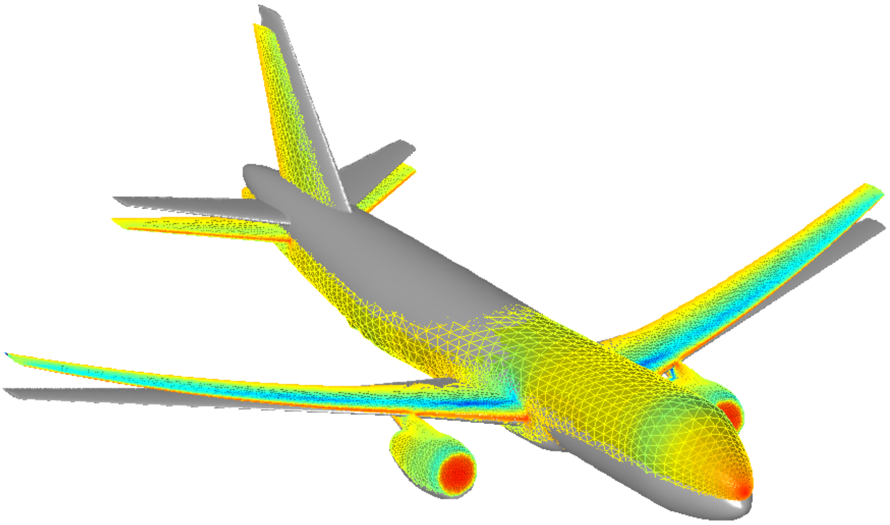

Figure 6.29: Deformed configuration of a trimmed A320, $M_\infty = 0.78$, $n = 1$

Concluding Remarks

The proposed independent fields formulation considerably simplifies the development of the numerical approximation of unsteady full potential flows, leading to a simple, precise and robust resolution scheme. Moreover, the developed improved density upwinding, by taking into account the geometry of the Mach cones at the element vertexes, avoids any numerical tuning and yields a continuous upwind activation, greatly contributing to the numerical stability of the method.

The adopted ALE formulation avoids any constraint to be imposed on the mesh motion to grant Geometric Conservation Law (GCL) so getting rid of any numerical complication related to the domain movement. Numerical results prove the effectiveness of the adopted approach in achieving the proper mass conservation without any special care for the choice of the integration scheme.

The independent fields approach simplifies also the formulation of a non isentropic FP model. The adoption of a thin entropy layer wrapping the body-wake and the related convected entropy equation ensure an effective unsteady correction, approaching Euler solutions. The related increase in the number of unknowns causes limited increase of the computational effort. The modified Laitone parameter proves the validity of the proposed stagnation pressure correction in affording a more physical shock position and strength, while adding to the two-field FP formulation a stabilization for otherwise possible non-unique solutions. Numerical results show the effectiveness of the entropy correction, for both steady and unsteady conditions.

To describe lifting bodies using a potential flow formulation a wake surface must be contained in the grid which discretizes the fluid surrounding the body. The tool realized to automatically embed a bounded surface, *i.e.* the wake, within a generic unstructured mesh makes it possible to avoid enforcing *ad hoc* mesh generations specifically adapted for potential flows and allows to simply model single or multiple wakes.

The node based unstructured finite volume discretization scheme uses linear|quadratic isoparametric shape functions and leads to a set of nonlinear ordinary differential equations. Time marching solutions can be obtained through first|second order implicit integration schemes, whose unconditional linearized stability properties have been demonstrated. Numerical results confirm the unconditional stability of the adopted implicit solvers, in sub-supersonic regions alike. The solution of the set of nonlinear algebraic equations uses a Newton-Raphson method with precise Jacobians. It is carried out through GMRES iterations, preconditioned with an incomplete *LU* factorization. The adopted preconditioner can even be related to an unperturbed condition and used for a set of Mach numbers, widely differing with respect to the one used for its calculation. Moreover, the same *LU* factorization can be used for homogeneous flow conditions to directly solve the system by simply iterating the related forward-backward substitutions a few times, with a significant gain of efficiency.

Numerical results well match analytical and alternative numerical solutions. The related calculation times should adequately depict the validity of the independent fields approach with respect to both simplicity and efficiency of the related unstructured numerical implementation. It should be noted also that a possible nonlinear unconditional stability can be inferred by the possibility of using very high CFL numbers for inaccurate transients responses leading to steady solutions. The moving least squares interface adopted to link the structural and the aerodynamic sub-systems in aeroelastic analyses proves its effectiveness for complex configuration such an A320 aircraft.

The proposed full-potential implementation combined with the adopted aeroelastic tools and the wake generation routine well satisfies the requirements that a CFD solver aimed to aeroelastic analyses must have in terms of both accuracy and efficiency.

Bibliography

[1] Murman, E. M. and Cole, J. D. Calculation of plane steady transonic flows. *AIAA Journal*, 9:114–121, 1971.

[2] Steger, J. L. and Lomax, H. Transonic flow about two-dimensional airfoils by relaxation procedures. *AIAA Journal*, 10:49–54, 1972.

[3] Garabedian, P. R. and Korn, D. Analysis of transonic airfoils. *Communications on Pure and Applied Mathematics*, 24:841–851, 1972.

[4] Ballhaus, W. F. and Bailey, F. R. Numerical calculation of transonic flow about swept wings. *AIAA Paper*, (72-677), 1972.

[5] Bailey, F. R. and Steger, J. L. Relaxation techniques for three-dimensional transonic flow about wings. *AIAA Paper*, (72-189), 1972.

[6] A. Jameson. Iterative solutions of transonic flows over airfoils and wings, including flows at mach 1. *Communications on Pure and Applied Mathematics*, 27:283–309, 1974.

[7] E. M. Murman. Analysis of embedded shockwaves calculated by relaxation methods. *AIAA Journal*, 12(5):626–635, 1974.

[8] A. Jameson. Transonic potential flow calculations using conservative form. *in Proceedings AIAA Second Computational Fluid Dynamics Conference. Hartford*, 1975.

[9] Glowinsky, R., Periaux, J., and Pironneau, O. Transonic flow simulation by the finite element method via optimal control. *Finite Elements in Fluids*, 3:249–259, 1976.

[10] Ecer, A. and Akay, H. U. Application of finite element method for the solution of transonic flow. *Finite Elements in Fluids*, 3:191–201, 1976.

[11] Jameson, A. and Caughey, D. A. Transonic potential flow calculations using conservative form. *in Proceedings AIAA Third Computational Fluid Dynamics Conference. Albuquerque*, 1977.

[12] Hafez, M. M., South, J. C., and Murman, E. M. Artificial compressibility methods for the numerical solution of the full potential equation. *AIAA Journal*, 17:838–844, 1978.

[13] A. Jameson. Acceleration of transonic potential flow calculations on arbitrary meshes by the multi-grid method. *AIAA Paper*, 79-1458, 1979.

[14] J. W. Boerstoel. A multi-grid algorithm for steady transonic potential flows around airfoils using newton iteration. *Journal Computational Physics*, 48:314–343, 1982.

[15] Van der Wees, A. J., Van der Vooren, J., and Meelker, J. H. Robust calculation of 3d transonic potential flow based on the non-linear fas multi-grid method and incomplete lu decomposition. *AIAA Paper*, 83-1950, 1983.

[16] Engquist, B. and Osher, S. Stable and entropy satisfying approximations for transonic flow calculations. *Mathematics of Computation*, 34:45–75, 1980.

[17] S. Osher. Shock modelling in aeronautics. *Numerical Methods for Fluid Dynamics. London*, pages 179–218, 1982.

[18] Volpe, G. and Jameson, A. Transonic potential flow calculations by two artificial density methods. *AIAA Paper*, 86-1084, 1986.

[19] T. L. Holst. Numerical solution of the full potential equation using a chimera grid approach. *NASA TM*, 110360, 1995.

[20] R. E. Neel. *Advances in Computational Fluid Dynamics: Turbulent Separated Flows and Transonic Potential Flows*. PhD thesis, Blacksburg, Virginia, 1997.

[21] Steger, J.L. and Baldwin, B.S. Shock waves and drag in the numerical calculation of isentropic transonic flow. *NASA TN*, D-6997, october 1972.

[22] Steger, J.L. and Baldwin, B.S. Shock waves and drag in the numerical calculation of compressible, irrotational transonic flow. *AIAA Journal*, 11(7):903–904, July 1973.

[23] Van der Vooren, J. and Slooff, J.W. On inviscid isentropic flow models used for finite difference calculations of two-dimensional transonic flows with embedded shocks about airfoils. *NLR MP 73024*, Aug. 1973.

[24] Murman, E.M. and Cole, J.D. Inviscid drag at transonic speeds. *AIAA Paper 74-540*, June 1974.

[25] Steinhoff, J. and Jameson, A. Multiple solutions of the transonic potential flow equation. *AIAA Journal*, 20:1521–1525, 1982.

[26] Salas, M. D. and Gumbert, C. R. Breakdown of the conservative potential equation. *AIAA Paper*, 85(0367), 1985.

[27] Klopfer, G.H. and Nixon, D. Nonisentropic potential formulation for transonic flows. *AIAA Journal*, 22(6):970–776, June 1984.

[28] C.W. Lucchi. Shock correction and trailing edge pressure jump in two-dimensional transonic potential flows at subsonic uniform mach numbers. *AIAA Paper 83-1884*, July 1983.

[29] Hafez, M. and Lovell, D. Entropy and vorticity corrections for transonic flows. *International Journal for Numerical Methods in Fluids*, 8:31–53, 1988.

[30] Whitlow, W. Jr., Hafez, M. M., and Osher, S. J. An entropy correction method for unsteady full potential flows with strong shocks. *AIAA Paper*, 86(1768-CP), 1986.

[31] Voss, R. and Wegner, W. Comparison of euler and full potential methods for unsteady transonic flow calculations. *AGARD Conference Proceedings 507, Transonic Unsteady Aerodynamics and Aeroelasticity*, March 1992.

[32] C. Hirsch. *Numerical Computation of Internal and Esternal Flows*. John Wiley Sons, New York, 1988.

[33] R. Chipman. An alternating-direction-implicit algorithm for the unsteady potential equation in conservation form. *NASA-CR-166152*, 1980.

[34] A. Parrinello. *Soluzione a due campi per Correnti a Potenziale Transoniche Instazionarie, Degree Thesis, Politecnico di Milano*. 2008.

[35] Timme, S. and Badcock, K. J. Transonic aeroelastic instability searches using sampling and aerodynamic model hierarchy. *AIAA Journal*, 49(6):1191–1201, 2011.

[36] Morino, L. and Gennaretti, M. Boundary integral equation methods for aerodynamics. *in S. N. Atluri (Ed.), Computational Nonlinear Mechanics in Aerospace Engineering, AIAA*, 146: Progress in Aeronautics and Astronautics:279–321, 1992.

[37] Guillard, H. and Farhat, C. On the significance of the geometric conservation law for flow computations on moving meshes. *Computer Methods in Applied Mechanics and Engineering*, 190:1467–1482, 2000.

[38] K.G. Guderley. The theory of transonic flow. *Pergamon Press, Oxford*, 1962.

[39] S. Timme. Transonic aeroelastic instability searches using a hierarchy of aerodynamic models. *University of Liverpool, degree of Doctor in Philosophy*, 2010.

[40] Parrinello, A. and Mantegazza, P. Independent two-fields solution for full-potential unsteady transonic flows. *AIAA Journal*, 48(7):1391–1402, 2010.

[41] E.V. Laitone. Limiting velocity by momentum relations for hydrofoils near the surface and airfoils in near sonic flow. *Proceedings of the Second U.S. National Congress of Applied Mechanics, P.M. Naghdi, et al., ed., ASME, New York*, 1955.

[42] E.V. Laitone. Local supersonic region on a body moving at subsonic speeds. *Symposium Transsonicum, K.Oswatitsch, ed., Springer-Verlag*, pages 57–70, 1964.

[43] W. H. Mason. On the use of the potential flow model for aerodynamic design at transonic speeds. *Aerospace Sciences Meeting and Exhibit, 33rd, Reno, NV*, Jan 9-12 1995.

[44] V. Shankar, H. Ide, and S. Osher. *A Fast Time-Accurate Unsteady Full Potential Scheme.* AIAA 7th Computational Fluid Dynamics Conference, 1985.

[45] M.J. Lighthill. On displacement thickness. *Journal of Fluid Mechanics*, 4(4):383–392, 1958.

[46] Fanion, T., Fernández, M. A., and Le Tallec, P. Deriving adequate formulations for fluid structure interaction problems: from ale to transpiration. *INSTITUT NATIONAL DE RECHERCHE EN INFORMATIQUE ET EN AUTOMATIQUE*, (3879):1391–1402, 2000.

[47] Zienkiewicz, O.C. and Taylor, R.L. *The Finite Element Method Fifth edition.* Butterworth-Heinemann, 2000.

[48] Masarati, P., Lanz, M., and Mantegazza, P. Multistep integration of ordinary, stiff and differential-algebraic problems for multibody dynamics applications. *XVI Congresso Nazionale AIDAA, Palermo*, pages 1–10, September 2001.

[49] Edwards, J. W. Unsteady aerodynamic modeling for arbitrary motions. *AIAA Journal*, 15(4):593–595, 1977.

[50] T. Theodorson. General theory of aerodynamic instability and the mechanism of flutter. *NACA TR-496*, 1935.

[51] Hassig, H.J. An approximate true damping solution of the flutter equation by determinant iteration. *Journal of Aircraft*, 8(11):885–889, 1971.

[52] Mantegazza, P. and Cardani, C. An iterative technique to compute flutter speed through the simultaneous solution of each aeroelastic mode and frequency at increasing speed. Aerotecnica Missili Spazio 54, 286-291, 1975.

[53] Cardani, C. and Mantegazza, P. Continuation and direct solution of the flutter equation. *Computers Structures*, 8:185–192, 1978.

[54] Davis, T. A. and Duff, I. S. An unsymmetric-pattern multifrontal method for sparse lu factorization. *SIAM Journal on Matrix Analysis and Applications*, 18(1):140–158, Jan. 1997.

[55] Earl H. Dowell. *A Modem Course in Aeroelas ticity, Third edition.* Kluwer Academic Publishers, 1995.

[56] Cavagna, L., Quaranta, G., Ghiringhelli, G. L., and Mantegazza, P. Efficient application of cfd aeroelastic methods using commercial software. *International Forum on Aeroelasticity and Structural Dynamics*, 2005.

[57] Cavagna, L., Quaranta, G., and Mantegazza, P. Aeroelasticità computazionale con modelli cfd. *Bollettino del Cilea 98*, 2005.

[58] Quaranta, G., Masarati, P., and Mantegazza, P. A conservative meshfree approach for fluid-structure problems. *Int. Conf. on Computational Methods for Coupled Problems in Science and Engineering*, 2005.

[59] Chwalowski, P., Florance, J. P., Heeg, J., Wieseman, C. D., and Perry, B. Preliminary computational analysis of the hirenasd configuration in preparation for the aeroelastic prediction workshop. *International Forum on Aeroelasticity and Structural Dynamics*, IFASD-2011-108.

[60] Zhongping Ji, Ligang Liu, Zhonggui Chen, and Guojin Wang. Easy mesh cutting. *Computer Graphics Forum*, 25(3):283–291, 2006.

[61] Juyong Zhang, Jianmin Zheng, and Jianfei Cai. Interactive mesh cutting using constrained random walks. *IEEE TRANSACTIONS ON VISUALIZATION AND COMPUTER GRAPHICS*, 17(3):357–367, 2011.

[62] Yong-Jin Liu, Dong-Liang Zhang, and Matthew Ming-Fai Yuen. A survey on cad methods in 3d garment design. *Computers in Industry*, 61:576–593, 2010.

[63] Bielser, D., Glardon, P., Teschner, M., and Gross, M. A state machine for real-time cutting of tetrahedral meshes. *Graphical Models*, 66:398–417, 2004.

[64] Romanelli, G., Serioli, E., and Mantegazza, P. A "free" approach to computational aeroelasticity. *48th AIAA Aerospace Sciences Meeting Including the New Horizons Forum and Aerospace Exposition*, 4 - 7 January 2010.

[65] Bisplinghoff, R. L., Ashely, H., and Halfman, R. L. *Aeroelasticity.* Dover, 1996.

[66] M. Martegani. *Un Metodo per il Calcolo del Flutter Linearizzato in Regime Transonico, Politecnico di Milano.* 2003.

[67] Schmitt, V. and Charpin F. Pressure distributions on the onera-m6-wing at transonic mach numbers. *Experimental Data Base for Computer Program Assessment. Report of the Fluid Dynamics Panel Working Group 04, AGARD AR 138*, May 1979.

[68] E. C. Yates. Agard standard aeroelastic configurations for dynamic response. i wing 445.6. *AGARD R 765*, 1985.

[69] M. Castellani. *Studio di una wing tip aeroelastica passiva, Degree Thesis, Politecnico di Milano.* 2011.